Deformation of fired clay material during rapid freezing due to supercooling

Fukui, Kazuma

Iba, Chiemi

Ogura, Daisuke

Title

Deformation of fired clay material during rapid freezing due to supercooling

Authors

Kazuma Fukui[1,*], Chiemi Iba[2], and Daisuke Ogura[2]

[1]Kobe University, Graduate School of Engineering, 1-1, Rokkodai-cho, Nada-ku, Kobe 657-8501, Japan

[2]Kyoto University, Graduate School of Engineering, Kyoto daigaku-katsura, Nishikyo-ku, Kyoto 615-8540, Japan

*Coresponding author

Email Address: fukui@peridot.kobe-u.ac.jp

Phone No: +81-78-803-6060

1 Introduction

Frost action is one of the main causes of the deterioration of porous building materials. A number of studies have investigated the deformation mechanisms and the resulting damage to predict deteriorations, propose proper countermeasures, and create frost-resistant materials (Powers, 1945; Penttala, 1998; Scherer & Valenza II, 2005). The freezing point depression of water in porous media is regarded as a non-negligible phenomenon in such studies (e.g., Hokoi, et al., 2000; Kočí, et al., 2017) and is anticipated from the pore radius assuming thermodynamic equilibrium (Fagerlund , 1973). However, liquid water in porous media can be supercooled and remain in a non-equilibrium liquid state even below the predicted freezing point. Among the studies on deformation and damage due to such frost action, some studies have pointed out the effects of supercooling. For instance, Grübl and Sotkin (1980) observed rapid expansion of cement-based materials accompanied by a sharp rise in temperature during the freezing of supercooled water. In addition, they showed that this rapid expansion had a good correlation with the residual strain after thawing. They considered that ice rapidly growing from the supercooled water can restrict the water movement in the material and cause the development of hydraulic pressure that results in instantaneous and residual expansion, referring to Powers' hypothesis (Powers, 1945). Based on their study, the freezing of supercooled water can affect the mechanical behavior of a material. Moreover, ice rapidly growing from supercooled water may cause more severe frost damage than relatively slow freezing near the thermodynamic equilibrium.

Although most of these studies investigated the supercooling effects on cement-based materials, supercooling can also affect the hygrothermal behavior of other building materials. For example, a delay of the start of the freezing process and rapid increase in the temperature of fired clay materials have been observed in both laboratory experiments and outdoor environments (Feng, et al., 2019; Iba, et al., 2016; Wardeh & Perrin, 2006, 2008), which is evidence of the presence of the supercooling phenomenon under various conditions, including the actual weather conditions.

Currently, it is becoming more important to understand the mechanisms of the deformation and damage of fired clay materials due to frost actions to deal with the increasing risks of frost damage on masonry walls associated with the internal insulation intended to improve the energy efficiency (Zhou, et al., 2017; Feng, et al., 2019) and preservation of ceramic bricks and tiles used for historical buildings (Iba, et al., 2016). Both fired clay and cement-based materials are considered frost-sensitive. Their frost resistance is highly dependent on the raw materials and manufacturing processes, e.g., mineral composition and firing temperature of fired clay materials (Maage 1984; Sánchez de Rojas et al., 2011) and water cement ratio and air content of cement-based materials. Similar to the concrete, Ranogajec et al. (2012) showed that damage to fired clay materials is caused by mechanisms such as hydraulic pressure, closed container, and ice lens mechanisms (Fagerlund, 1997); however, due to their large permeability, roofing tiles sintered at normal temperatures (around 1000 °C) suffer from the ice lens

mechanism rather than the well-known Power's hydraulic pressure theory. In addition, owing to the pressing prosses, the destruction of fired clay materials is characterized by delamination and anisotropic cracks (Perrin et al., 2011).

However, despite the great effort to investigate the mechanisms of the deformation and frost damage of fired clay materials (Iba, et al., 2016; Wardeh & Perrin, 2006, 2008, 2011; Ducman, et al., 2011; Sánchez de Rojas et al., 2011; Ranogajec et al., 2012), the effects of supercooling on the deformation have not been examined in detail. The effects of supercooling on the deformation of the fired clay materials should be investigated separately from cement-based materials because of the large differences in pore structures and hygrothermal and mechanical properties. In addition, the supercooled water in a fired clay material freezes much faster than that in cement-based materials (Fukui, et al., 2020, 2021), which can lead more significant pressure development in a material.

While we examined the hygrothermal behavior of a fired clay material during the freezing of the supercooled water, as presented in previous papers (Fukui, et al., 2020, 2021), we investigated the effects of supercooling on the deformation, as presented herein, using both experimental and numerical approaches. First, we conducted a freeze–thaw experiment to measure the strain evolution of the material during freezing and thawing. Subsequently, we developed a coupled hygrothermal and mechanical model of the freezing and thawing processes, including supercooling. The model was based on a poromechanical approach established by Coussy (2004). Models based on poromechanics have been developed in (Koniorczyk, et al., 2015; Koniorczyk, 2015; Eriksson, et al., 2018; Zeng, et al., 2011; Zeng, et al., 2016) but have been validated only for small cement-based materials with dimensions of several millimeters. Therefore, we validated the model by comparing the calculated strain evolution with the measurement results using a relatively large specimen. Using the model, we examined the processes of water movement, phase change, pressure development, and deformation during freezing, including the supercooling process, and demonstrated the decisive factors of the magnitude of the effects of supercooling on the deformation.

2 Methods

2.1. Experiments

2.1.1. Material

In this study, the material used was made from clay produced in Aichi Prefecture, Japan, which is commonly used in producing tiles in the area. The sintering temperature of clay was 1000 °C. The material is plated-shaped with a thickness of approximately 20 mm and is considered as transversely isotropic, similar to common roof tiles (Stolecki, et al., 1999).

Figure 1 shows the logarithmic differential pore volume distribution of the material measured using mercury intrusion porosimetry (Fukui, et al., 2021). The figure also exhibits the freezing point of water in the pores theoretically determined based on the thermodynamic equilibrium between the ice and liquid water (Brun, et al., 1977). Moreover, for comparison, we showed the pore volume distribution of the cement paste with the water-cement ratio of 0.4 and an age of more than 1 year. The material contained pores with diameters larger than those of cement-based materials (Diamond, 1971; Cook & Hover, 1999). Therefore, most of the water contained in the pores is subject to a lower capillary pressure, and the freezing point depression is not significant.

[insert Figure 1]

2.1.2. Strain measurement

The schematic of the specimen used for strain measurement is shown in Fig. 2. We used a rectangle specimen with a bottom surface of 46.4 × 94.7 mm and a height of 21.0 mm. The height direction of the specimen corresponded to the thickness direction of the material. Strain gages and thermocouples were attached with cyanoacrylate adhesive to the center of the top surface and one of the sides with a dimension of 21.0 × 94.7 mm. The strain was measured in a direction that was parallel and normal to the height direction on the side and top surfaces with a dimension of 21.0 × 94.7 mm, respectively, to check the anisotropy of the material. The employed strain gages were KFLB-5-120-C1-11 R3M3 (Kyowa Electronic Instruments Co., Ltd, Japan). After the strain gages and thermocouples were attached, the specimen was vacuum-saturated and then loosely covered with plastic wrap to prevent evaporation from the surfaces but not to constrain the deformation, allowing the movement of liquid water. It was confirmed that the thermal resistance of the plastic wrap was negligible before the experiment. The air temperature in the test chamber was maintained at 293 K (20 °C) for 30 min to stabilize the temperature distribution in the specimen before the cooling started. Subsequently, the specimen was cooled at a minimum air temperature of 253 K (−20°C) for 4 h and heated at the maximum air temperature of 293 K (20°C) for 4 h. The experiment consisted of six freeze-thaw cycles. The set points of the air temperature in the test chamber were changed in a stepwise manner at the beginning of the cooling and heating periods. During measurement, the temperature and strain of the specimen and the air temperature in the test chamber were recorded every second.

[insert Figure 2]

2.2. Coupled hygrothermal and mechanical modeling

Here, we develop a numerical model corresponding to the freeze-thaw experiment to examine the deformation processes during the freezing of supercooled water.

2.2.1. Constitutive equations

Although most of the numerical simulations of the freeze-thaw processes of building materials have been conducted using an isotropic model, it is considered that the anisotropy of the properties of fired clay materials has considerable effects on its mechanical behavior. Therefore, in this study, we developed a model that considered the anisotropy (transverse isotropy) of the elastic modulus and water transfer. The constitutive equations of the saturated porous media are expressed as (Coussy, 2004):

$$\boldsymbol{\sigma} = \mathbf{D}\left[\boldsymbol{\varepsilon} - \boldsymbol{\alpha}\left(T - T_r\right)\right] - \mathbf{b}p \ , \tag{1}$$

$$\varphi = \mathbf{b} : \boldsymbol{\varepsilon} + \frac{p}{N} - \alpha_\phi \left(T - T_r\right), \tag{2}$$

where $\mathbf{b}$ is the Biot tangent tensor, $\mathbf{D}$ is the material elastic stiffness tensor [Pa], N is the Biot tangent modulus [Pa], p is the pressure [Pa], T is the temperature [K], T_r is the reference temperature [K], $\boldsymbol{\alpha}$ is the tensor of the thermal expansion coefficient of the skeleton [K^{-1}], α_ϕ is the volumetric thermal expansion coefficient related to the porosity [K^{-1}], $\boldsymbol{\varepsilon}$ is the strain tensor, φ is the increment of the porosity, and $\boldsymbol{\sigma}$ is the total stress tensor [Pa].

For the freezing and thawing of the porous media, the ice and liquid water pressures should be considered separately.

$$\boldsymbol{\sigma} = \mathbf{D}\left[\boldsymbol{\varepsilon} - \boldsymbol{\alpha}\left(T - T_r\right)\right] - \left(\mathbf{b_i} p_i + \mathbf{b_l} p_l\right), \tag{3}$$

$$\varphi_i = \mathbf{b_i} : \boldsymbol{\varepsilon} + \frac{p_i}{N_{ii}} + \frac{p_l}{N_{il}} - a_i \left(T - T_r\right) \qquad \varphi_l = \mathbf{b_l} : \boldsymbol{\varepsilon} + \frac{p_i}{N_{li}} + \frac{p_l}{N_{ll}} - a_l \left(T - T_r\right), \tag{4}$$

where a_j is a coefficient related to the volumetric thermal expansion of the pore volume occupied by each phase [K^{-1}] and N_{ii}, N_{il}, N_{li}, and N_{ll} are the generalized Biot coupling moduli [Pa]. Here, the subscripts i and l represent ice and liquid water, respectively. For simplicity, $\mathbf{b_i}$ and $\mathbf{b_l}$ are expressed as proportional values for the saturation S of each phase, according to literature (Coussy, 2005; Coussy & Monteiro, 2008).

$$\mathbf{b_j} = \mathbf{b}S_j \qquad j = i, l \tag{5}$$

The anisotropies of $\mathbf{b}$ and $\boldsymbol{\alpha}$ are ignored in this study. They are represented by values b and α, respectively. Therefore, the final form of the constitutive equations used in this study are expressed as

$$\boldsymbol{\sigma} = \mathbf{D}\left[\boldsymbol{\varepsilon} - \alpha\left(T - T_r\right)\mathbf{I}\right] - b\left(S_i p_i + S_l p_l\right)\mathbf{I}\ , \tag{6}$$

$$\varphi_i = b\varepsilon_v + \frac{p_i}{N_{ii}} + \frac{p_l}{N_{il}} - a_i\left(T - T_r\right) \qquad \varphi_l = b\varepsilon_v + \frac{p_i}{N_{li}} + \frac{p_l}{N_{ll}} - a_l\left(T - T_r\right), \tag{7}$$

where b is the Biot coefficient, $\mathbf{I}$ is the second-order unit tensor, α is the thermal expansion coefficient [K^{-1}], and ε_v is the volumetric strain.

The poroelastic parameters in Eqs. (6) and (7) to be determined are a_i, a_l, b, N_{ii}, N_{il}, N_{li}, and N_{ll}. We obtained b, N_{ii}, N_{il}, N_{li}, and N_{ll} by assuming that the Young's modulus in the height direction of the specimen was much smaller than that in the normal direction ($E_t << E_v$, where E_t and E_v are the Young's moduli in the direction that is parallel and normal to the height, respectively) or the strain in the direction normal to the height was considerably small to obtain b, N_{ii}, N_{il}, N_{li}, and N_{ll}. This assumption leads to the relationship $b = 1 - E_t/E_s$, where E_s is the Young's modulus of the solid phase. Helmuth and Turk (1966) derived the relationship $E_t/E_s = (1 - \phi)^3$ for hardened cement paste, where ϕ is the porosity. Then, N_{ii}, N_{il}, N_{li}, and N_{ll} were calculated using the equations derived by Aichi and Tokunaga (2011). Equation (8) is obtained using the relationship $E_t << E_v$.

$$\frac{1}{N_{ll}} \approx \frac{b - \phi_0}{E_s} S_l^2 \qquad \frac{1}{N_{li}} = \frac{1}{N_{il}} \approx \frac{b - \phi_0}{E_s} S_l S_i \qquad \frac{1}{N_{ii}} \approx \frac{b - \phi_0}{E_s} S_i^2 \tag{8}$$

where ϕ_0 is the porosity in a reference state.

In (Coussy, 2004), the derivation of a_i and a_l for anisotropic materials were not reported. Given that the anisotropy of the thermal expansion of the solid volume was ignored in this study, we assumed that a_j did not exhibit strong anisotropy. Therefore, a_i and a_l are derived from Eq. (9) by assuming the isotropy of the material (Coussy, 2004).

$$a_j = 3\alpha\left(b - \phi_0\right)S_j \qquad j = i, l \tag{9}$$

Finally, the main simplifications used in the constitutive equations in this study is summarized as follows:

- The plastic deformation of the material was not considered.
- $\mathbf{b_i}$ and $\mathbf{b_l}$ were set to be proportional to S_i and S_l, respectively, as shown in Eq. (5) (Coussy, 2005; Coussy & Monteiro, 2008).

- The anisotropy of b and α was ignored.
- The simplified forms of the poroelastic parameters a_i, a_l, b, N_{ii}, N_{il}, N_{li}, and N_{ll} are given. This is expected since the material used in this study had strong anisotropy, and our main concern was the mechanical behavior in the height direction of the specimen, which is the most deformable.

2.2.2. Liquid-ice relationship under equilibrium and non-equilibrium conditions

The Clausius–Clapeyron equation derived from the equilibrium of the chemical potential of liquid and ice ($\mu_i = \mu_l$, where μ is the chemical potential) is expressed in Eq. (10) (Coussy & Monteiro, 2009).

$$\frac{p_l}{\rho_l} - \frac{p_i}{\rho_i} = \frac{\Delta s}{\rho_i}\left(T - T_m\right), \tag{10}$$

where T_m is the melting point of bulk water [K], Δs is the melting entropy (Δs=1.2 [MPa/K]), and ρ is the density [kg/m^3]. The dependency of ρ_i and ρ_l on p and T is expressed in a linearized form (Coussy, 2005; Coussy & Monteiro, 2008).

$$\frac{1}{\rho_j} = \frac{1}{\rho_j^0}\left(1 - \frac{p_j}{K_j} + 3\alpha_j\left(T - T_r\right)\right) \quad j = i, l \tag{11}$$

where K is the bulk modulus and ρ^0 is the density in the reference state.

S_l can be expected from the pressure difference between ice and liquid under thermodynamic equilibrium conditions. The equation suggested by van Genuchten (1980) is as follows:

$$S_l = \left[\frac{1}{1 + \left(\beta\left(p_i - p_l\right)\right)^n}\right]^m. \tag{12}$$

Models presented in (Koniorczyk, et al., 2015; Gawin, et al., 2019) consider the hysteresis during freezing and thawing caused by the difference in the shape of the interface between liquid water and ice. However, we focused on the freezing process, where the water is supercooled, in the calculation. Accordingly, the equilibrium freezing and thawing processes in the calculation were not distinguished, that is, hysteresis was not considered.

Under non-equilibrium states, Eqs. (10) and (12) cannot be used because they are based on thermodynamic equilibrium. Therefore, the rate of the increase of ice saturation ($\partial Si/\partial t$) was derived from the general kinetic equation.

$$\frac{dS_i}{dt} = A\exp\left(-\frac{E_a}{RT}\right) f\left(S_i\right), \tag{13}$$

where A is a constant [s^{-1}], E_a is the activation energy [J/mol], $f(S_i)$ is a function of the ice saturation ($=S_i^a(1-S_i)^b$, where a and b are constants), R is the gas constant (= 8.314 [J/(K·mol)]), and t is time [s]. The parameters in Eq. (13) were calibrated using the results of differential scanning calorimetry as follows: $A = 9.71 \times 10^{-9}$ s^{-1}, $E_a = -36694$ J/mol, $a = 0.68$, and $b = 1.12$ (Fukui, et al., 2021).

Models presented in (Koniorczyk, et al., 2015; Gawin, et al., 2019) consider non-equilibrium states (relatively close to the equilibrium). In these models, the Young-Laplace equation was used to relate the current liquid water saturation of a material and the pressure difference between the ice and liquid water. To the best of our knowledge, there are no studies that have reported the applicability of the assumption of the mechanical equilibrium for the large pressure difference and rapid penetration of ice into liquid-filled pores under strong non-equilibrium states, that is, during the freezing of supercooled water. Based on Eq. (6), the evolution of p_i does not significantly contribute to the stress when S_i is not large. In fact, the increase in S_i during the non-equilibrium freezing was 0.11 to 0.14, which will be mentioned in Section 4, and is not significant. Therefore, we used Eq. (12) even under non-equilibrium conditions assuming that the calculation results were not significantly influenced by the relationship between p_i and p_l.

2.2.3. Conservation equations

The momentum balance is expressed as

$$\nabla \cdot \boldsymbol{\sigma} + \mathbf{F} = 0\,, \tag{14}$$

where $\mathbf{F}$ is the body force vector [N/m^3]. $\mathbf{F} = 0$ because we did not consider any sources of external force.

Equations for the heat and moisture mass conservation can be expressed as follows:

$$\frac{\partial}{\partial t}\left(CT - Hm_i\right) = \nabla \cdot \left(\boldsymbol{\lambda} \nabla T\right), \tag{15}$$

$$\frac{\partial}{\partial t}\left(m_i + m_l\right) = \nabla \cdot \left(\boldsymbol{\lambda}' \nabla p_l\right), \tag{16}$$

where

$$m_i = \rho_i\left(\phi_0 S_i + \varphi_i\right) \quad m_l = \rho_l\left(\phi_0 S_l + \varphi_l\right), \tag{17}$$

$$C = c_d \rho_d + c_i m_i + c_l m_l\,. \tag{18}$$

Here, c is the specific heat [J/(kg·K)], H is the latent heat of solidification (= 334 × 10^3 [J/kg]), $\boldsymbol{\lambda}$ is the tensor of thermal conductivity [W/(m·K)], and $\boldsymbol{\lambda}'$ is the tensor of moisture permeability related to the liquid water pressure gradient [kg/(m·s·Pa)]. The subscript d represents the bulk material in the dry state. C is the volumetric specific heat of the wet material [J/(m^3·K)], and m_i and m_l are the masses of the ice and liquid water, respectively, contained in a unit volume of the bulk material [kg/m^3].

2.2.4. Calculation methods for freeze–thaw processes including supercooling

We began the calculation using the temperature above the freezing point to reproduce the temperature distribution in the specimen when freezing started. Therefore, the calculation included three states: unfrozen, non-equilibrium freezing, and equilibrium freezing. The calculation method accounting for these three states was similar to that in previous studies (Fukui, et al., 2020, 2021), in which we developed a hygrothermal model including supercooling processes. However, the conditions under which the state of water changes to another state were slightly different because we accounted for the p_i evolution in this study.

Figure 3 shows the conditions under which water state changes. While the freezing of a saturated material is expected to start when the temperature drops below T_m under thermodynamic equilibrium conditions, the start of freezing is delayed when the water is supercooled. We set the temperature T_f [K] at which the supercooled water started to freeze to a value measured in the freeze-thaw experiment. In addition, previous studies (Fukui, et al., 2020, 2021) reported that the solidification of supercooled water in the fired clay material starts almost simultaneously in a specimen. Therefore, in the calculations, the freezing of a segment is triggered when it comes into contact with a segment containing ice.

[insert Figure 3]

The S_i of the material rapidly increases after the supercooled water starts freezing, as shown in Eq. (13). On the other hand, S_l decreases based on Eq. (16), and the difference between p_i and p_l changes, as expected from Eq. (12). Furthermore, T increases because of the released latent heat, as shown in Eq. (15). The thermodynamic equilibrium of the water in the material is achieved when Eq. (10) is satisfied.

During the heating period, the state of the water in the material changed directly from the equilibrium freezing state to the unfrozen state when S_i decreased to 0.

2.2.5. Calculation model, conditions, and numerical solution

The calculation model for the strain measurement is shown in Fig. 4. The calculation was performed two-dimensionally on a cross-section with a size of 40 × 20 mm under the assumption of the plane

strain state. Given that the specimen was symmetric, the calculation was conducted on a quarter of the cross-section, and the two axes of the rectangular coordinate system were set in the directions of the 40 mm and 20 mm sides (x and y axes in Fig. 4, respectively). The basic equations were discretized using the Galerkin finite element method for space with 2 × 2 mm bilinear elements based on the monolithic approach. The calculation results were confirmed to not be dependent on the mesh size by comparing these results using the elements with half sides. T, p_l, and displacement vector $\mathbf{u}$ [m] were expressed using vectors of the nodal values $\mathbf{T}_e$, $\mathbf{p}_e$, and $\mathbf{u}_e$, respectively, and the shape function $\mathbf{N}$ and $\mathbf{N}_u$.

$$T = \mathbf{N}\mathbf{T}_e \quad p_l = \mathbf{N}\mathbf{p}_e \quad \mathbf{u} = \mathbf{N}_u\mathbf{u}_e \tag{19}$$

After the discretization, we obtained the following system of equations:

$$\begin{bmatrix} \mathbf{C}_{TT} & \mathbf{C}_{Tp} & \mathbf{C}_{Tu} \\ \mathbf{C}_{pT} & \mathbf{C}_{pp} & \mathbf{C}_{pu} \\ \mathbf{C}_{uT} & \mathbf{C}_{up} & \mathbf{C}_{uu} \end{bmatrix} \frac{\partial}{\partial t} \begin{bmatrix} \mathbf{T}_e \\ \mathbf{p}_e \\ \mathbf{u}_e \end{bmatrix} = \begin{bmatrix} \mathbf{K}_{TT} & \mathbf{0} & \mathbf{0} \\ \mathbf{0} & \mathbf{K}_{uu} & \mathbf{0} \\ \mathbf{0} & \mathbf{0} & \mathbf{0} \end{bmatrix} \begin{bmatrix} \mathbf{T}_e \\ \mathbf{p}_e \\ \mathbf{u}_e \end{bmatrix} + \begin{bmatrix} \mathbf{f}_T \\ \mathbf{f}_p \\ \partial \mathbf{f}_u / \partial t \end{bmatrix}, \tag{20}$$

where Eq. (6) was differentiated by time. All components in Eq. (20) are presented in the Appendix. The discretization in time was performed using the finite difference method. The forward difference was used and the time step was set to 0.00125 s. We confirmed that the calculation was stable with no oscillations. The program code was developed by the authors using programming language Fortran 90.

[insert Figure 4]

Table 1 summarizes the initial and boundary conditions. The initial temperature was assumed to be uniform in the material. It was set as the average of the two temperatures measured on the top and side surfaces at the beginning of the freeze-thaw experiment. Considering that the specimen was completely saturated, the initial value of p_l in the material was set to 0 Pa. On the axes of symmetry (x = 0 or y = 0 in Fig. 4), no heat or moisture flow was considered, and the displacement normal to the direction of the axis was restricted. During the experiment, the evaporation of water through the surface of the material was prevented by plastic wrap, but the wrap did not restrict liquid water movement through the surfaces. Therefore, p_l on the surface of the material was set to 0 Pa. The Robin boundary condition with the measured temperature of the air in the test chamber was used to calculate the heat flux density on the surface of the material. The heat transfer coefficient was set to 6.5 [W/(m^2·K)] to ensure that the calculation results of the temperature evolution is in agreement with the measurement results.

Table 1. Initial and boundary conditions of the calculation.

	Position	Coordinate (shown in Fig. 4)	Heat	Moisture	Stress and displacement
Initial condition	Calculation area	$0 \le x \le L_x$ and $0 \le y \le L_y$	Measured temperature	$p_l = 0$	$\mathbf{u} = 0$
Boundary condition	Axes of the symmetry	$x = 0$ or $y = 0$	$\mathbf{Q} \cdot \mathbf{n} = 0$	$\mathbf{J} \cdot \mathbf{n} = 0$	$\mathbf{u} \cdot \mathbf{n} = 0$
	Material's surfaces	$x = L_x$ or $y = L_y$	$\mathbf{Q} \cdot \mathbf{n} = h\,(T - T_{out})$	$p_l = 0$	$\boldsymbol{\sigma} \cdot \mathbf{n} = 0$

h is the heat transfer coefficient [W/(m^2·K)]; **J** and **Q** are vectors of the moisture flow [kg/(m^2·s)] and heat flow [W/m^2], respectively; **n** is a unit vector normal to the boundary; T_{out} is the air temperature measured in the test chamber [K]

2.2.6 Material properties

Table 2 lists the material properties with constant values. Some of these properties were derived in our previous study (Fukui, et al., 2021). A thermomechanical analysis on an air-dried specimen was conducted to determine α. The shear modulus G_{tv} [Pa] was calculated using the following equation (Hayashi, 1954):

$$\frac{1}{G_{tv}} = \frac{4}{E_{45}} - \left(\frac{1}{E_t} + \frac{1}{E_v} - \frac{\nu_{tv}}{E_t} \right), \tag{21}$$

where E_{45} is the Young's modulus in the 45° direction from the height direction [Pa] and ν_{tv} is the Poisson's ratio corresponding to the loading in the normal direction. G_{tv} was obtained by assuming that E_{45} was the average of E and E'. We adopted the value of a brick from (Kumaran, 1996) for c_d.

Table 2. Material properties with a constant value.

Property	Unit	Direction	Symbol	Value	Source
Dry density	kg/m^3		ρ_s	1800	Measurement
Water content at vacuum saturation (regarded as porosity)	m^3/m^3		ϕ_0	0.299	Measurement
Specific heat	J/(kg·K)		c_d	840	(Kumaran, 1996)
Young modulus	Pa	Height	E_t	3×10^9	Measurement
		Normal to the height	E_v	11×10^9	Measurement
Shear modulus	Pa		G_{tv}	5×10^9	Equation (21)
Poisson's ratio		*1	ν_{tv}	0.12	Measurement
			ν_{vt}	0.44	
			ν_{vv}	0.19	
Thermal expansion coefficient	K^{-1}		α	2.91×10^{-6}	Measurement

*1 A symbol ν_{mn} represents the Poisson's ratio that corresponds to an expansion in direction n when a contraction is applied in direction m.

The relationship between air pressure p_a [Pa] and p_l in an unsaturated material and between p_i and p_l in a frozen material can be expressed using the Young–Laplace equation:

$$p_a - p_l = 2\frac{\gamma_{al}}{r}, \tag{22}$$

$$p_i - p_l = 2\frac{\gamma_{il}}{r}, \tag{23}$$

where r is the pore radius [m], and γ_{al} and γ_{il} are the interfacial energies between the air and liquid water (= 73×10^{-3} J/m^2 at 20 °C) and between the ice and liquid water (= 33×10^{-3} J/m^2 at 0 °C (Ketcham & Hobbs, 1969)), respectively. The difference in p_a–p_l in Eq. (22) is the negative value of the capillary pressure p_c [Pa]. Moreover, S_l of a frozen material can be obtained from the adsorption isotherm of an unfrozen and unsaturated material using Eqs. (22) and (23).

$$S_l = \left[\frac{1}{1 + \left(\beta \frac{\gamma_{al}}{\gamma_{il}} \left(p_i - p_l \right) \right)^n} \right]^m \tag{24}$$

289 The adsorption isotherm of the employed material in the unfrozen state was derived in our previous
290 study (Fukui, et al., 2021) based on gas adsorption and pressure plate methods. The constants β, n, and
291 m in Eq. (12) were determined to be 1.1×10^{-6} Pa^{-1}, 2.3, and 0.57, respectively. The hysteresis of S_l
292 was not considered in the calculations.
293 Data on the thermal conductivity and moisture permeability of the material were available in our
294 previous study (Fukui, et al., 2021). For simplicity, we ignored the anisotropy of $\boldsymbol{\lambda}$. Therefore, the
295 thermal conductivity of the material was represented by one value λ. The following linear relationship
296 was derived from the measurement of the thermal conductivity of the air-dried and wet materials using
297 the transient hot wire method (Fukui, et al., 2021):

298 $$\lambda = 1.26 S_l + 0.55 \,. \tag{25}$$

299 Equation (26) was used to calculate the thermal conductivity during the freezing and thawing
300 processes.

301 $$\lambda = 1.26 \left(S_l + \frac{\lambda_i}{\lambda_l} S_i \right) + 0.55 \tag{26}$$

302 In this calculation, we considered the anisotropy of the water permeability, Young's modulus, and
303 Poisson's ratio. We obtained the moisture permeability in the direction normal to the height direction
304 using the Boltzmann transformation and gamma-ray attenuation method (Fukui, et al., 2021). However,
305 the gamma-ray attenuation method is not suitable for measurements in the height direction because
306 the material was too thin (only approximately 20 mm). Therefore, we conducted mass measurements
307 during water absorption to compare the water absorption coefficient and average moisture diffusivity,
308 which was proportional to the square of the water absorption coefficient (Kumaran, 1999), in the
309 parallel and normal directions. Based on the results, the average moisture diffusivity was 2.1 times
310 smaller in the height direction than in the normal direction. Then, we assumed that the water
311 permeability in the height direction was 2.1 times smaller in the entire saturation range.
312 Finally, we present the equilibrium relationship derived from Eq. (24) and the moisture
313 permeability in Fig. 5. The liquid water content ψ_l [m^3/m^3] and water chemical potential μ [J/kg] for
314 free water in the previous study (Fukui, et al., 2021) were re-expressed using the saturation degree of
315 liquid water S_l (= ψ_l / ϕ) and water pressure (= $\mu\rho_l$), respectively, to calculate these properties.

316 [insert Figure 5]

317 In this subsection, the full set of material properties used to conduct the numerical analysis is shown.
318 Therefore, the heat transfer coefficient between the specimen surfaces and air in the test chamber was
319 the only calibrated parameter. In the next section, we verify the numerical model by comparing the
320 calculated and measured strains of the freeze-thaw experiment. Then, we investigate the supercooling

effects on the deformation of the fired clay material.

3 Results

3.1. Freeze-thaw experiment

Figures 6 and 7 present the results of the strain measurements during the first freeze-thaw cycle. The strain evolution during subsequent cycles is not exhibited in the figures because it did not change drastically, except for the development of the plastic strain. From the figures, the strain measured both on the side (in the y-axis direction) and top surface (in the x-axis direction) are shown, but the temperature on the top surface is omitted in Fig. 6 because it was almost the same as that on the side surface. Moreover, we presented the strain referring to the values at a temperature of 20 °C during the cooling process, as indicated by the triangle.

[insert Figure 6]

[insert Figure 7]

The results of the strain measurement show expansion due to freezing. The start of the expansion was delayed because of supercooling until the temperature reached −4.8 °C, as shown by the dotted squares in Fig. 6 (a). The temperature rapidly increased to slightly less than 0 °C at the same time as the strain increased. The increase in strain was only a small value (0.0479×10^{-3} in the y-axis direction). The strain in the y-axis direction then decreased and increased as the temperature decreased during the cooling period. Conversely, the strain measured in the x-axis direction continued to decrease after expansion, which indicates the strong anisotropy of the deformation.

3.2. Coupled hygrothermal and mechanical simulation

Figure 8 shows the comparison of the calculation results, which do not include the supercooling process with the measurement results. In this calculation, the non-equilibrium freezing state in Fig. 3 was omitted during the cooling process, and the state of water directly changed from unfrozen to equilibrium freezing. Therefore, Eq. (10) was used throughout the freezing process. The rapid temperature rise and expansion associated with the freezing of the supercooled water could not be reproduced although the trends of the calculated and measured temperature and strain evolutions are generally in agreement, except for the strain evolutions on the top surface (in the x-axis direction). This difference on the top surface may be attributed to the anisotropy of the Biot coefficient; however, the deformation of the top surface is small and its influence on the deformation of the side surface is considered insignificant. The difference in the magnitude of the measured and calculated strain evolution on the side surface may be due to inaccuracies in the material properties used in the

352 calculation, such as the water permeability and adsorption isotherm.

353 [insert Figure 8]

354 Figures 9 and 10 show the calculated temperature and strain using a model that includes
355 supercooling. In addition, the calculated ice saturation evolution using the model including the
356 supercooling process are presented in Figs. 11 and 12. The ice saturation at two different distances
357 from the center of the specimen along the x-axis is shown ((x, y) = (0.005, 0) and (0.015, 0) in the
358 coordinate shown in Fig. 4). The calculated temperature adequately reproduced the rapid rise observed
359 in the experiment while the calculation results did not significantly change except for those when the
360 supercooled water started freezing (at an elapsed time of approximately 1 h and 30 min). During the
361 increase of the temperature, the calculated strain also rapidly increased as the measured strain although
362 subsequent decrease in the calculated strain was much faster than the measured strain. The rapid
363 increase in the calculated temperature and strain was 7–8 min later than that of the measured
364 temperature and strain, which is probably because of imperfections in the material properties used in
365 the calculation, such as the thermal conductivity, adsorption isotherm, and estimation of the heat
366 transfer coefficient between the surfaces of the specimen and air in the test chamber.

367 [insert Figure 9]

368 [insert Figure 10]

369 [insert Figure 11]

370 [insert Figure 12]

371 **4 Discussion**

372 **4.1. Effects of supercooling on the deformation of a fired clay material**

373 During the experiment, the increase in strain during the rapid temperature increase was much smaller
374 than that associated with the subsequent temperature decrease in the y-axis direction. Based on these
375 results, the effects of supercooling on the deformation of the fired clay material were small.

376 The temperature of the specimen rapidly increased to approximately 0 °C during the experiment.
377 A further increase in temperature was not observed, which indicated that the rapid ice formation
378 stopped at that time. The temperature that was reached when the temperature stopped increasing was
379 interpreted as the equilibrium temperature without supercooling effects (Grübl & Sotkin, 1980).
380 Therefore, it is expected that the ice growth and resulting expansion were restricted by the equilibrium
381 freezing temperature as the upper limit of the temperature rise accompanied by ice growth in the
382 experiment.

Grübl and Sotkin (1980), who conducted freeze-thaw experiments using cement-based materials, showed that the remaining expansion after thawing had a good correlation with the rapid expansion associated with non-equilibrium freezing. However, in our experiment, the residual strain after thawing (1.28×10^{-3}) was considerably larger than the rapid increase in the strain (0.0479×10^{-3}) in the y-axis direction. Therefore, it is considered that the supercooling effects on the damage were also small in the fired clay material, and the subsequent expansion associated with the temperature decrease caused the residual strain instead. The supercooled water in the fired clay material freezes much faster than that in cement-based materials (Fukui, et al., 2020, 2021). As discussed by Grübl and Sotkin (1980), the ice rapidly growing from the supercooled water can restrict the water movement in a material and cause development of the hydraulic pressure resulting in instantaneous and residual expansion. Therefore, it is possible that greater pressure occurs in the fired clay material because of the more rapid volume change of the water than that in cement-based materials. The reasons for the small expansion of the fired clay material caused by the freezing of supercooled water are discussed in the following subsection.

4.2. Mechanisms of the deformation with and without supercooling

The varieties of ice saturation in the material were relatively small, and 11%–14 % of water solidified during the non-equilibrium freezing, as shown in Figs. 11 and 12. This amount of freezing water can cause significant liquid pressure if the material is sealed (Coussy & Monteiro, 2009). Therefore, it is expected that the pressure developed by freezing was relaxed because of the transfer of liquid water toward the surfaces of the material.

We conducted an additional calculation in which the water permeability was set to a 0.1 times larger value than that in the calculation described previously to examine the contribution of the water transfer to the strain and pressure evolution in the material. Figures 13 and 14 show the calculated liquid pressure and strain evolution, respectively. A much greater pressure takes place, and it takes longer to relax the pressure in the case of a small water permeability when the liquid pressure increases and then drops rapidly when using the original water permeability. Furthermore, Fig. 14 shows that the increase in strain is much greater than that in the original calculation shown in Fig. 9.

[insert Figure 13]

[insert Figure 14]

Therefore, the pressure developed owing to the rapid ice growth during the freezing of the supercooled water can be relaxed by the liquid water transfer, and it does not cause significant deformation if the material has sufficient water permeability. It is also probable that the difference in

415 the water permeability can cause a difference in the magnitude of the supercooling effects among the
416 materials.
417 Finally, Fig. 15 shows the calculated evolution of the liquid water and ice pressure during the entire
418 freezing and thawing processes using the model including the supercooling process and original water
419 permeability. In contrast to the pressure evolution during the non-equilibrium freezing shown in Fig.
420 13, the pressure develops significantly during equilibrium freezing as the temperature decreases and
421 ice saturation increases. The water permeability of the material decreases, accompanied by a decrease
422 in the liquid water saturation, preventing water from escaping toward the surface of the material. In
423 addition, the ice pressure is even higher than that of liquid water because of the relationship expressed
424 in Eq. (10). Therefore, the pressure evolution caused by the small water permeability after the
425 considerable amount of water solidified, and the ice pressure increases because of the chemical
426 potential equilibrium causing deformation in the fired clay material, rather than rapid ice growth
427 during non-equilibrium freezing.

428 [insert Figure 15]

429 **5 Conclusion**

430 In this study, we investigated the effects of supercooling on the deformation of a fired clay material
431 using strain measurements and coupled hygrothermal and mechanical simulations based on the
432 poromechanical approach. During the experiment, the specimen was maintained to be saturated by
433 preventing evaporation using a plastic wrap with negligible thermal resistance. The wrap loosely
434 covered the specimen surfaces to avoid constraining the deformation, allowing liquid water seepage.
435 During the measurement, the temperature rapidly increased, and an increase in the strain associated
436 with the freezing of the supercooled water was apparent. However, this increase in the strain was only
437 small (0.0479×10^{-3} in the thickness direction of the material). Conversely, after the rapid freezing of
438 the supercooled water stopped, the strain in the thickness direction of the material increased
439 significantly as the temperature decreased. From these results, we concluded that the effects of
440 supercooling on deformation are small on the fired clay material compared to cement-based materials
441 reported in literature (Grübl & Sotkin, 1980). In addition, the supercooling effects on the damage were
442 small and the subsequent expansion associated with the temperature decrease caused the residual strain
443 because the residual strain after thawing was considerably larger than the rapid increase in the strain
444 associated with the freezing of the supercooled water.
445 Based on the comparison of the results of the strain measurement and calculated pressure and strain
446 evolution, the reasons for the small impacts of supercooling on the deformation of the fired clay
447 material are as follows:

- The temperature of a material with a relatively large volume (i.e., specimen for the strain measurement) rapidly increases after the supercooled water starts freezing because the released latent heat cannot easily escape from the surfaces of the material. This rapid temperature increase is then restricted by the equilibrium freezing temperature, resulting in the restriction of the growth of ice and the resulting pressure.
- Based on the comparison of the calculation results with different moisture permeabilities, the small impact of supercooling on deformation can be due to the sufficiently large moisture permeability of the fired clay material. The increased pressure associated with the freezing of the supercooled water is relaxed by the water transfer toward the surfaces of the material, even though the supercooled water in the fired clay material freezes much faster than that in cement-based materials (shown in our previous study (Fukui, et al., 2021)). It is also shown that the effect of supercooling can be more significant if a material has a low moisture permeability.

Further studies need to be conducted to reveal the impacts of supercooling on the deformation and damage of materials with various material properties, especially of those with low water permeability (e.g., cement-based materials). The freezing rates and degree of the freezing point depression also affects the significance of the supercooling, and their combined effects should be discussed. The strain measurements and numerical simulations were conducted under single temperature and moisture conditions. However, studies under conditions closer to the outdoor environment should be conducted to evaluate the effects of supercooling on real building components.

Appendix

The components in Eq. (20) are defined as follows:

$$\mathbf{C}_{\mathbf{TT}} = \int_{\Omega} \frac{\partial}{\partial T}\left(CT - H_{li} m_i\right) \mathbf{N}^T \mathbf{N} d\Omega \,, \tag{A.1}$$

$$\mathbf{C}_{\mathbf{Tp}} = \int_{\Omega} \frac{\partial}{\partial p_l}\left(CT - H m_i\right) \mathbf{N}^T \mathbf{N} d\Omega \,, \tag{A.2}$$

$$\mathbf{C}_{\mathbf{Tu}} = \int_{\Omega} \frac{\partial}{\partial \varepsilon_v}\left(CT - H m_i\right) \mathbf{N}^T \mathbf{m}^T \mathbf{B} d\Omega \,, \tag{A.3}$$

$$\mathbf{C}_{\mathbf{pT}} = \int_{\Omega} \frac{\partial}{\partial T}\left(m_i + m_l\right) \mathbf{N}^T \mathbf{N} d\Omega \,, \tag{A.4}$$

$$\mathbf{C}_{\mathbf{pp}} = \int_{\Omega} \frac{\partial}{\partial p_l}\left(m_i + m_l\right) \mathbf{N}^T \mathbf{N} d\Omega \,, \tag{A.5}$$

475 $$\mathbf{C_{pu}} = \int_{\Omega} \frac{\partial}{\partial \varepsilon_v}\left(m_i + m_l\right)\mathbf{N}^T \mathbf{m}^T \mathbf{B} d\Omega\,, \tag{A.6}$$

476 $$\mathbf{C_{uT}} = -\int_{\Omega}\left[\alpha \mathbf{B^T D} + b\frac{\partial}{\partial T}\left(S_i p_i + S_l p_l\right)\mathbf{B^T}\right]\mathbf{m}\mathbf{N} d\Omega\,, \tag{A.7}$$

477 $$\mathbf{C_{up}} = -\int_{\Omega} b\frac{\partial}{\partial p_l}\left(S_i p_i + S_l p_l\right)\mathbf{B^T}\mathbf{m}\mathbf{N} d\Omega\,, \tag{A.8}$$

478 $$\mathbf{C_{uu}} = \int_{\Omega} \mathbf{B^T D B} d\Omega\,, \tag{A.9}$$

479 $$\mathbf{K_{TT}} = \int_{\Omega} \nabla \mathbf{N}^T \boldsymbol{\lambda} \nabla \mathbf{N} d\Omega + \int_{\Gamma} h \mathbf{N}^T d\Gamma\,, \tag{A.10}$$

480 $$\mathbf{K_{pp}} = \int_{\Omega} \nabla \mathbf{N}^T \boldsymbol{\lambda}' \nabla \mathbf{N} d\Omega\,, \tag{A.11}$$

481 where Ω and Γ are the domain of an element and its boundary, respectively, and

482 $$\mathbf{m} = \begin{bmatrix} 1 & 1 & 0 \end{bmatrix}^T\,, \tag{A.12}$$

483 $$\mathbf{B} = \begin{bmatrix} \frac{\partial N_1}{\partial x_1} & 0 & \frac{\partial N_2}{\partial x_1} & 0 & \frac{\partial N_3}{\partial x_1} & 0 & \frac{\partial N_4}{\partial x_1} & 0 \\ 0 & \frac{\partial N_1}{\partial x_2} & 0 & \frac{\partial N_2}{\partial x_2} & 0 & \frac{\partial N_3}{\partial x_2} & 0 & \frac{\partial N_4}{\partial x_2} \\ \frac{\partial N_1}{\partial x_2} & \frac{\partial N_1}{\partial x_1} & \frac{\partial N_2}{\partial x_2} & \frac{\partial N_2}{\partial x_1} & \frac{\partial N_3}{\partial x_2} & \frac{\partial N_3}{\partial x_1} & \frac{\partial N_4}{\partial x_2} & \frac{\partial N_4}{\partial x_1} \end{bmatrix}. \tag{A.13}$$

484 During the unfrozen and equilibrium freezing states

485 $$\mathbf{f_T} = -\int_{\Gamma}\left(Q - hT_{out}\right)\mathbf{N}^T d\Gamma\,, \tag{A.15}$$

486 $$\mathbf{f_P} = -\int_{\Gamma} J\mathbf{N}^T d\Gamma\,, \tag{A.16}$$

487 $$\frac{\partial \mathbf{f_u}}{\partial t} = \frac{\partial}{\partial t}\int_{\Gamma} \mathbf{N_u}^T \mathbf{t} d\Gamma\,, \tag{A.17}$$

488 where **t** is the external force vector [N/m^2]. During the non-equilibrium freezing state, $\partial S_i/\partial t$ was

489 directly given by Eq. (13). In this case, Eqs. (A.15) to (A.17) were altered by Eqs. (A.18) to (A.20).

490 $$\mathbf{f}_{\mathbf{T}} = -\int_{\Gamma}\left(Q - \alpha T_{out}\right)\mathbf{N}^{T}d\Gamma - \int_{\Omega}\frac{\partial}{\partial S_i}\left(CT - Hm_i\right)\frac{\partial S_i}{\partial t}\mathbf{N}^{T}\mathbf{N}d\Omega \tag{A.18}$$

491 $$\mathbf{f}_{\mathbf{p}} = -\int_{\Gamma} J\mathbf{N}^{T}d\Gamma - \int_{\Omega}\frac{\partial}{\partial S_i}\left(m_i + m_l\right)\frac{\partial S_i}{\partial t}\mathbf{N}^{T}d\Omega \tag{A.19}$$

492 $$\frac{\partial \mathbf{f}_{\mathbf{u}}}{\partial t} = \frac{\partial}{\partial t}\int_{\Gamma}\mathbf{N}^{T}\mathbf{t}d\Gamma + \int_{\Omega} b\frac{\partial}{\partial S_i}\left(S_i p_i + S_l p_l\right)\frac{\partial S_i}{\partial t}\mathbf{B}^{T}\mathbf{m}^{T}d\Omega \tag{A.20}$$

493 **References**

494 Aichi, M. & Tokunaga, T., 2011. Thermodynamically consistent anisotropic constitutive relations
495 for a poroelastic material saturated by two immiscible fluids. *International Journal of Rock*
496 *Mechanics & Mining Sciences,* Volume 48, pp. 580-84.

497 Brun, M., Lallemand, A., Quinson, J. & Eyraud, C., 1977. A new method for the simultaneous
498 determination of the size and the shape of pores: the thermoporometry. *Thermochimica Acta,*
499 Volume 21, pp. 59-88.

500 Cook, R. A. & Hover, K. C., 1999. Mercury porosimetry of hardened cement pastes. *Cement and*
501 *Concrete Research,* Volume 29, pp. 933-43.

502 Coussy, O., 2004. *Poromechanics.* s.l.:John Wiley & Sons.

503 Coussy, O., 2005. Poromechanics of freezing materials. *Journal of the Mechanics and Physics of*
504 *Solids,* Volume 53, pp. 1689-1718.

505 Coussy, O. & Monteiro, P. J., 2008. Poroelastic model for concrete exposed to freezing
506 temperatures. *Cement and Concrete Research,* Volume 38, pp. 40-48.

507 Coussy, O. & Monteiro, P. J., 2009. Errata to "Poroelastic model for concrete exposed to freezing
508 temperatures. *Cement and Concrete Research,* Volume 39, pp. 371-72.

509 Diamond, S., 1971. A critical comparison of mercury porosimetry and capillary condensation pore
510 size distributions of Portland cement pastes. *Cement and Concrete Research,* Volume 1, pp. 531-
511 45.

512 Ducman, V., Škapin, A. S., Radeka, M. & Ranogajec, J., 2011. Frost resistance of clay roofing tiles:
513 case study. *Ceramics International,* Volume 37, pp. 85-91.

514 Eriksson, D., Gasch, T., Malm, R. & Ansell, A., 2018. Freezing of partially saturated air-entrained
515 concrete: A multiphase description of the hygro-thermo-mechanical behaviour. *International*
516 *Journal of Solids and Structures,* Volume 152-53, pp. 294-304.

517 Fagerlund, G., 1973. Determination of pore-size distribution from freezing-point depression.
518 *Materials and Structures,* Volume 6, pp. 215-25.

519 Fagerlund, G., 1997. *Internal frost attack-state of the art: suggestions for future research (Report*

520 *TVBM (Intern 7000-rapport); Vol. 7110).* Lund: Division of Building Materials, LTH, Lund
521 University.
522 Feng, C., Roels, S. & Janssen, H., 2019. Towards a more representative assessment of frost damage
523 to porous building materials. *Building and Environment,* Volume 164, p. 106343.
524 Fukui, K. et al., 2020. Experimental investigation and hygrothermal modelling of freeze-thaw
525 process of saturated fired clay materials including supercooling phenomenon. In: *Proceedings of*
526 *the 12th Nordic Symposium of Building Physics.* s.l.:s.n.
527 Fukui, K. et al., 2021. Investigation into the hygrothermal behavior of fired clay materials during the
528 freezing of supercooled water using experiments and numerical simulations. *Journal of Building*
529 *Physics,* https://doi.org/10.1177/17442591211041144.
530 Gawin, D., Pesavento, F., Koniorczyk, M. & Schrefler, B. A., 2019. Non-equilibrium modeling
531 hysteresis of modeling hysteresis of thawing in partially saturated porous building materials.
532 *Journal of Building Physics,* Volume 43, pp. 61-98.
533 Grübl, P. & Sotkin, A., 1980. Rapid ice formation in hardened cement paste, mortar and concrete
534 due to supercooling. *Cement and Concrete Research,* Volume 10, pp. 333-45.
535 Hayashi, T., 1954. On the elastic properties of an orthogonal-anisotropic plate having the principal
536 axes of elasticity slanted to its edges. *Journal of the Japan Society of Aeronautical Engineering,*
537 Volume 2, pp. 12-17.
538 Helmuth, R. A. & Turk, D. H., 1966. Elastic moduli of hardened portland cement and tricalcium
539 silicate pastes: effect of porosity. *Highway Research Board, Special Report,* Volume 90, pp. 135-
540 44.
541 Hokoi, S., Hatano, M., Matsumoto, M. & Kumaran, M. K., 2000. Freezing-Thawing Processes in
542 Glass Fiber Board. *Journal of Thermal Envelope and Building Science,* Volume 24, pp. 42-60.
543 Iba, C., Ueda, A. & Hokoi, S., 2016. Field survey on frost damage to roof tiles under climatic
544 conditions. *Structural Survey,* Volume 34, pp. 135-49.
545 Ketcham, W. M. & Hobbs, P. V., 1969. An experimental determination of the surface energies of
546 ice. *Philosophical Magazine,* Volume 19, pp. 1161-73.
547 Kočí, J., Maděra, J., Keppert, M. & Černý, R., 2017. Damage functions for the cold regions and their
548 applications in hygrothermal simulations of different types of building structures. *Cold Regions*
549 *Science and Technology,* Volume 135, pp. 1-7.
550 Koniorczyk, M., 2015. Coupled heat and water transport in deformable porous materials considering
551 phase change kinetics. *International Journal of Heat and Mass Transfer,* Volume 81, pp. 260-71.
552 Koniorczyk, M., Gawin, D. & Schrefler, B. A., 2015. Modeling evolution of frost damage in fully
553 saturated porous materials exposed to variable hygro-thermal conditions. *Computer Methods in*
554 *Applied Mechanics and Engineering,* Volume 297, pp. 38-61.

555 Kumaran, M. K., 1996. *IEA Annex 24, Final Report, Vol. 3, Task 3: Material Properties.* Leuven:
556 Laboratorium Bouwfysica, Department Burgerlijke Bouwkunde, KU Leuven.
557 Kumaran, M. K., 1999. Moisture diffusivity of building materials from water absorption
558 measurements. *Journal of Thermal Envelope and Building Science,* Volume 22, pp. 349-55.
559 Maage, M., 1984. Frost resistance and pore size distribution in bricks. *Materials and Structures,*
560 Volume 17, pp. 345-50.
561 Penttala, V., 1998. Freezing-induced strains and pressures in wet porous materials and especially in
562 concrete mortars. *Advanced Cement Based Materials,* Volume 7, pp. 8-19.
563 Perrin, B., Vu, N. A. Multon, S., Voland, T., & Ducroquetz, C., 2011. Mechanical behaviour of fired
564 clay materials subjected to freeze–thaw cycles. *Construction and Building Materials,* Volume 25,
565 pp. 1056-64.
566 Powers, T. C., 1945. A working hypothesis for further studies of frost resistance of concrete. *Journal*
567 *of the American Concrete Institute,* Volume 16, pp. 245-72.
568 Ranogajec, J., Kojić, P., Rudić, O., Ducman, V., & Radeka, M., 2012. Frost action mechanisms of clay
569 roofing tiles: case study. *Journal of Materials in Civil Engineering,* Volume 24, pp. 1254-60.
570 Sánchez de Rojas, M. I., Marín, F. P., Frías, M., Valenzuela, E. & Rodríguez, O., 2011. Influence of
571 freezing test methods, composition and microstructure on frost durability assessment of clay
572 roofing tiles. *Construction and Building Materials,* Volume 25, pp. 2888-97.
573 Scherer, G. W. & Valenza II, J. J., 2005. Mechanisms of frost damage. In: *Materials Science of*
574 *Concrete VII.* s.l.:American Ceramic Society, pp. 209-46.
575 Stolecki, J., Piekarczyk, J. & Rudnik, T., 1999. Heterogeneity and anisotropy of ceramic roof tiles.
576 *British Ceramic Proceedings,* Volume 60, pp. 383-84.
577 Van Genuchten, M. T., 1980. A Closed-form Equation for Predicting the Hydraulic Conductivity of
578 Unsaturated Soils. *Soil Science Society of America Journal,* Volume 44, pp. 892-98.
579 Wardeh, G. & Perrin, B., 2006. Analysis of strains in baked clay based materials during freezing and
580 thawing cycles. *Journal of Building Physics,* Volume 29, pp. 201-17.
581 Wardeh, G. & Perrin, B., 2008. Freezing–thawing phenomena in fired clay materials and
582 consequences on their durability. *Construction and Building Materials,* Volume 22, pp. 820-28.
583 Zeng, Q., Fen-Chong, T., Dangla, P. & Li, K., 2011. A study of freezing behavior of cementitious
584 materials by poromechanical approach. *International Journal of Solids and Structures,* Volume
585 48, pp. 3267-73.
586 Zeng, Q., Li, K. & Fen-Chong, T., 2016. Effect of supercooling on the instantaneous freezing
587 dilation of cement-based porous materials. *Journal of Building Physics,* Volume 40, pp. 101-24.
588 Zhou, X., Derome, D. & Carmeliet, J., 2017. Hygrothermal modeling and evaluation of freeze-thaw
589 damage risk of masonry walls retrofitted with internal insulation. *Building and Environment,*
590 Volume 125, pp. 285-98.

591

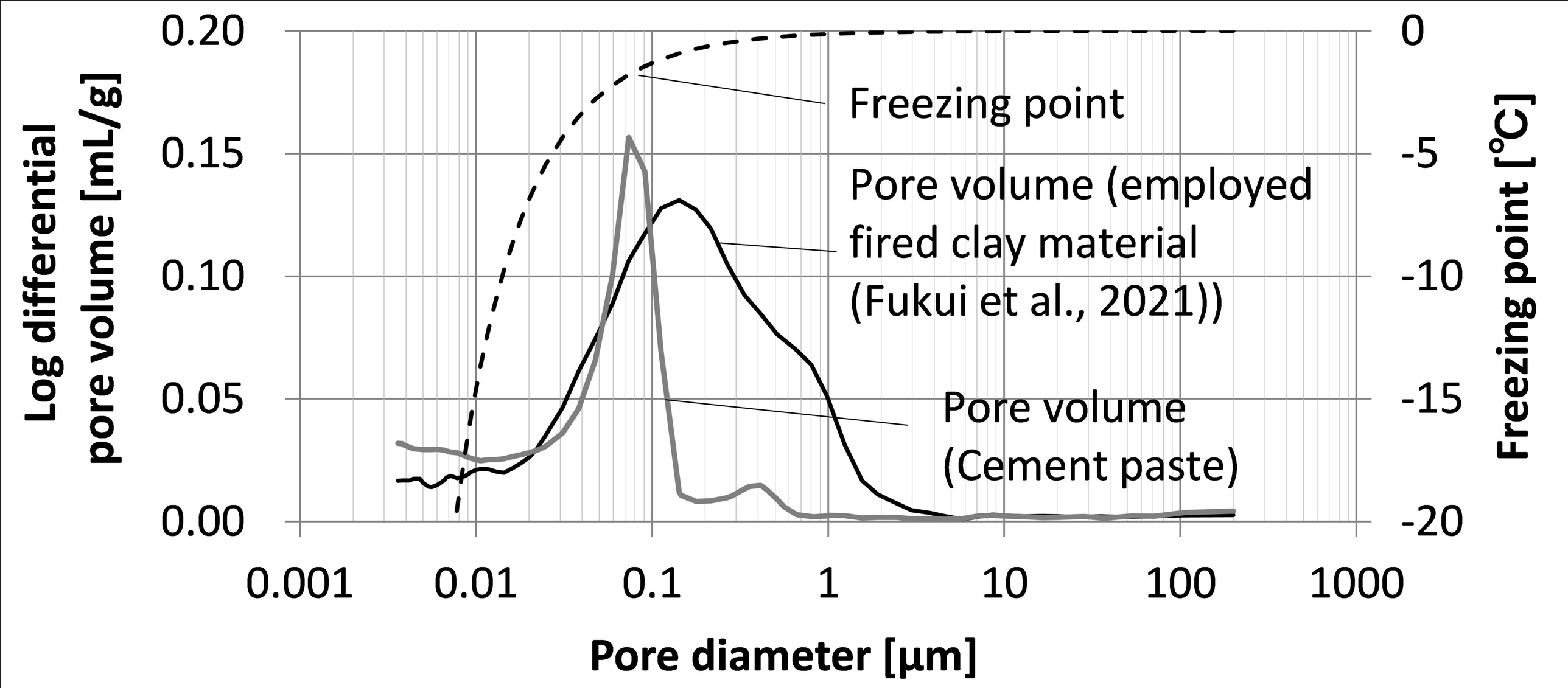
0.20
0.15
0.10
0.05
0.00
Log differential pore volume [mL/g]
0
-5
-10
-15
-20
Freezing point [°C]
Freezing point
Pore volume (employed fired clay material (Fukui et al., 2021))
Pore volume (Cement paste)
0.001
0.01
0.1
1
10
100
1000
Pore diameter [µm]

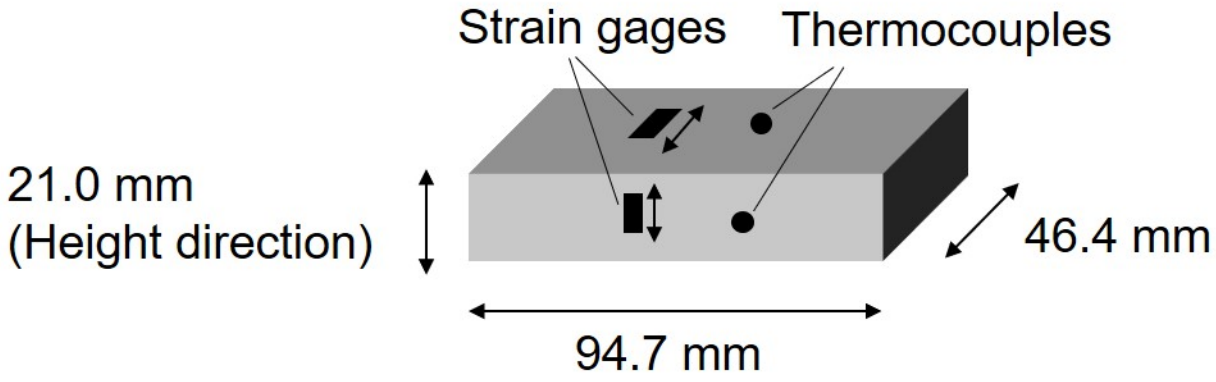
Strain gages
Thermocouples
21.0 mm
(Height direction)
46.4 mm
94.7 mm

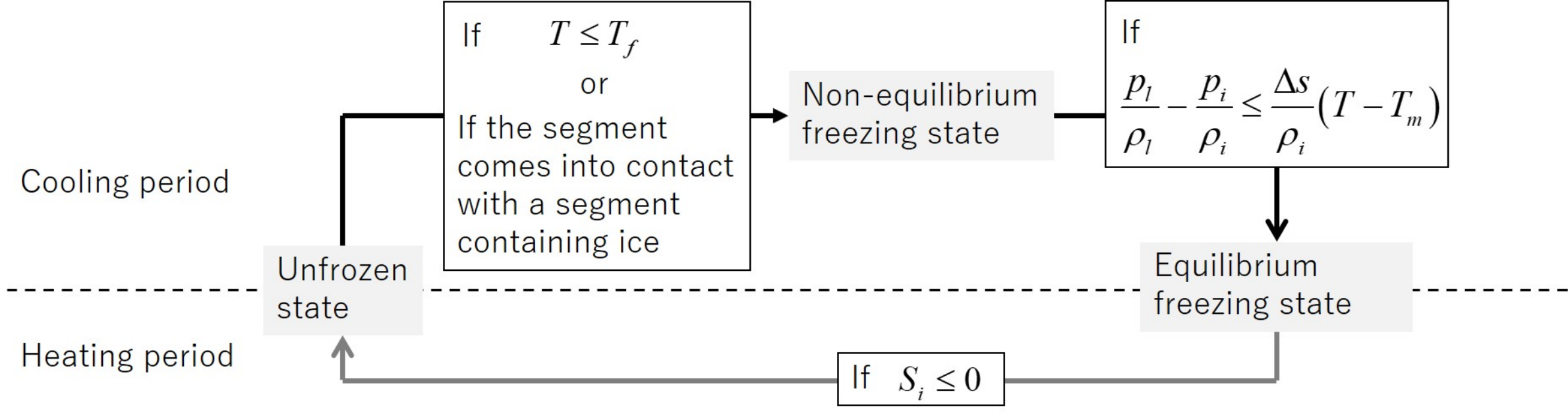
Cooling period
Heating period
Unfrozen state
If $T \le T_f$
or
If the segment comes into contact with a segment containing ice
Non-equilibrium freezing state
If $\frac{p_l}{\rho_l} - \frac{p_i}{\rho_i} \le \frac{\Delta s}{\rho_i}(T - T_m)$
Equilibrium freezing state
If $S_i \le 0$

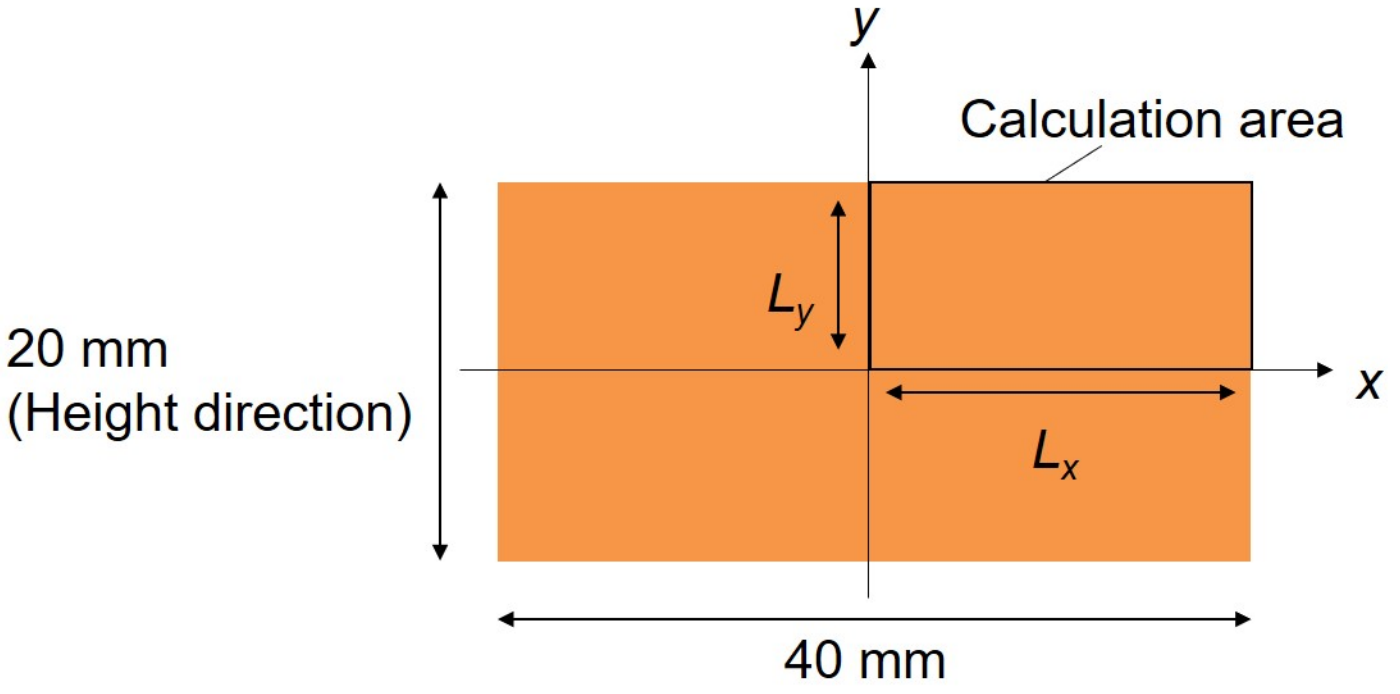
y
Calculation area
L_y
20 mm
(Height direction)
x
L_x
40 mm

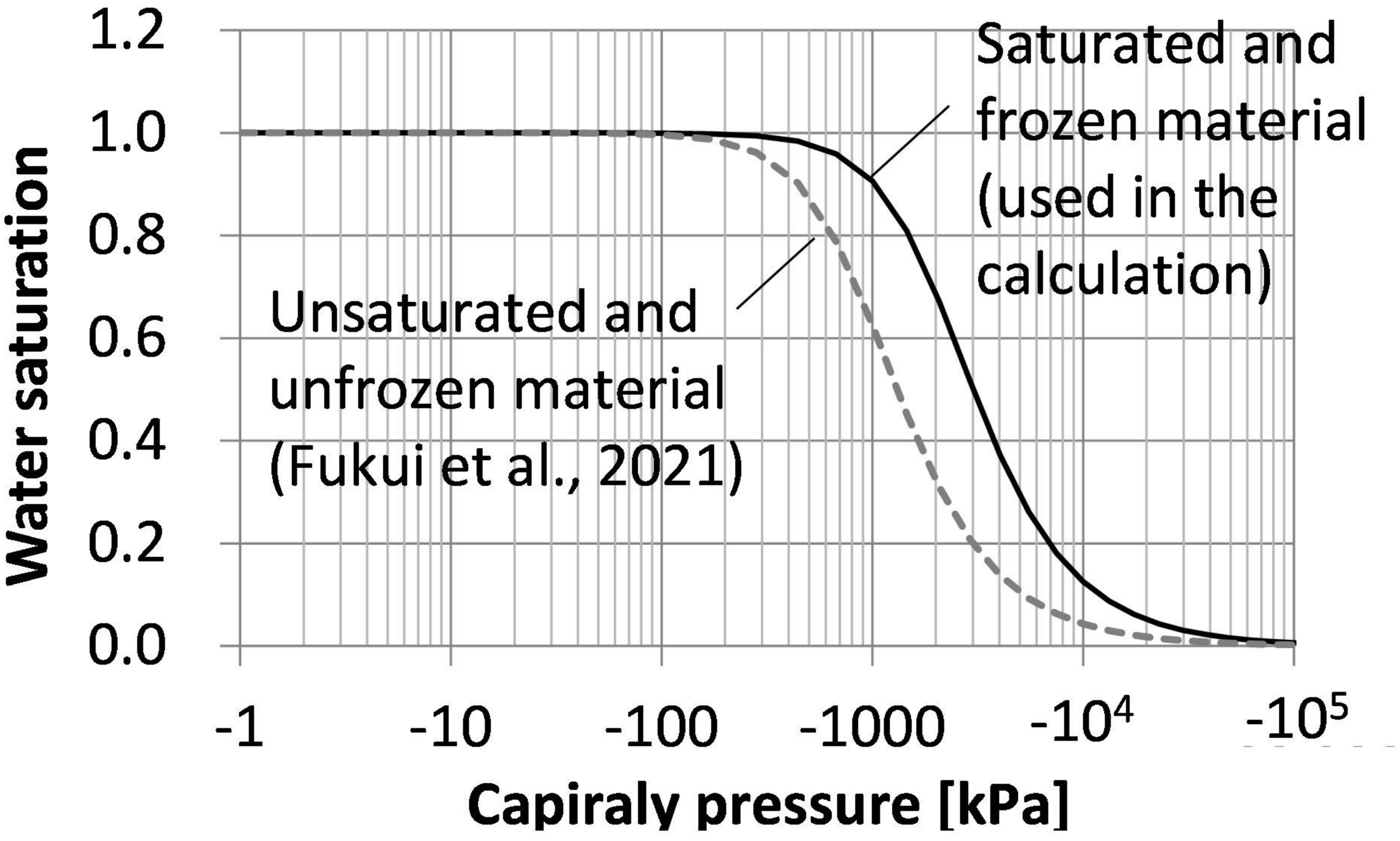
Water saturation
1.2
1.0
0.8
0.6
0.4
0.2
0.0
Saturated and frozen material (used in the calculation)
Unsaturated and unfrozen material (Fukui et al., 2021)
-1
-10
-100
-1000
-10^4
-10^5
Capiraly pressure [kPa]

(a)

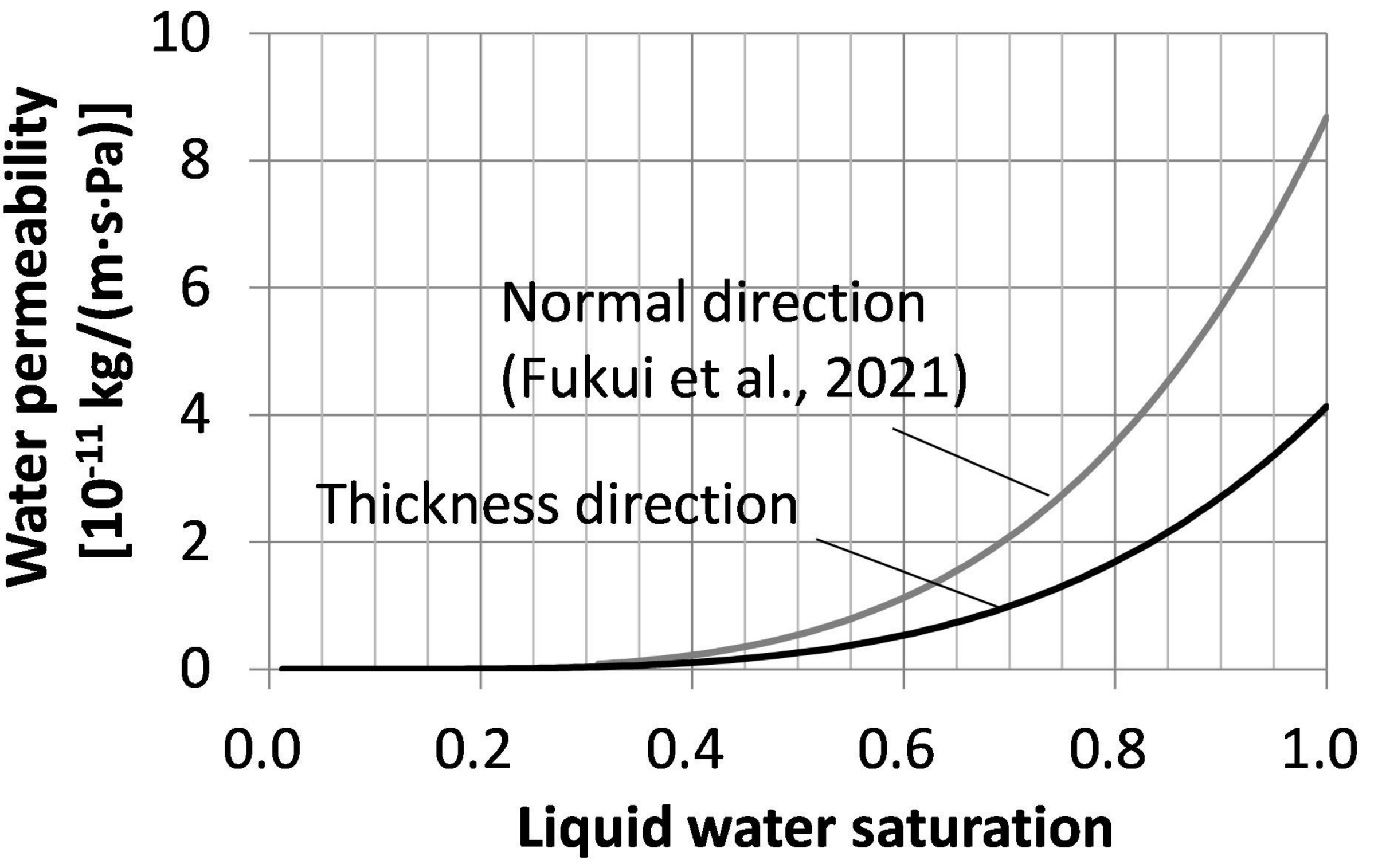
Water liquid permeability
[10^-11 kg/(m·s·Pa)]
10
8
6
4
2
0
Normal direction (Fukui et al., 2021)
Thickness direction
0.0
0.2
0.4
0.6
0.8
1.0
Liquid water saturation

(b)

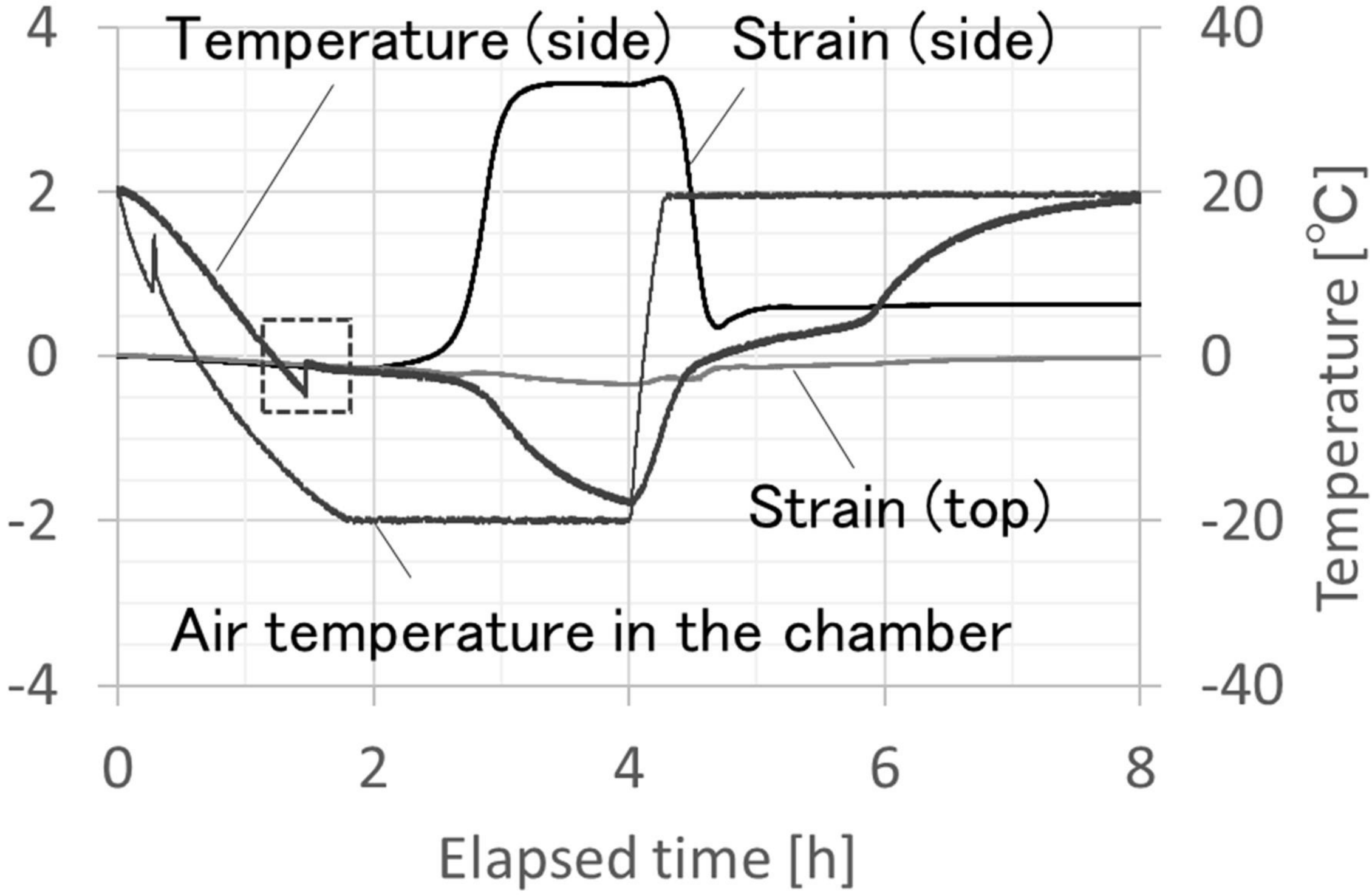
Temperature (side)
Strain (side)
Strain (top)
Air temperature in the chamber
Strain [10-3]
Temperature [°C]
Elapsed time [h]
4
2
0
-2
-4
40
20
0
-20
-40
0
2
4
6
8

(a)

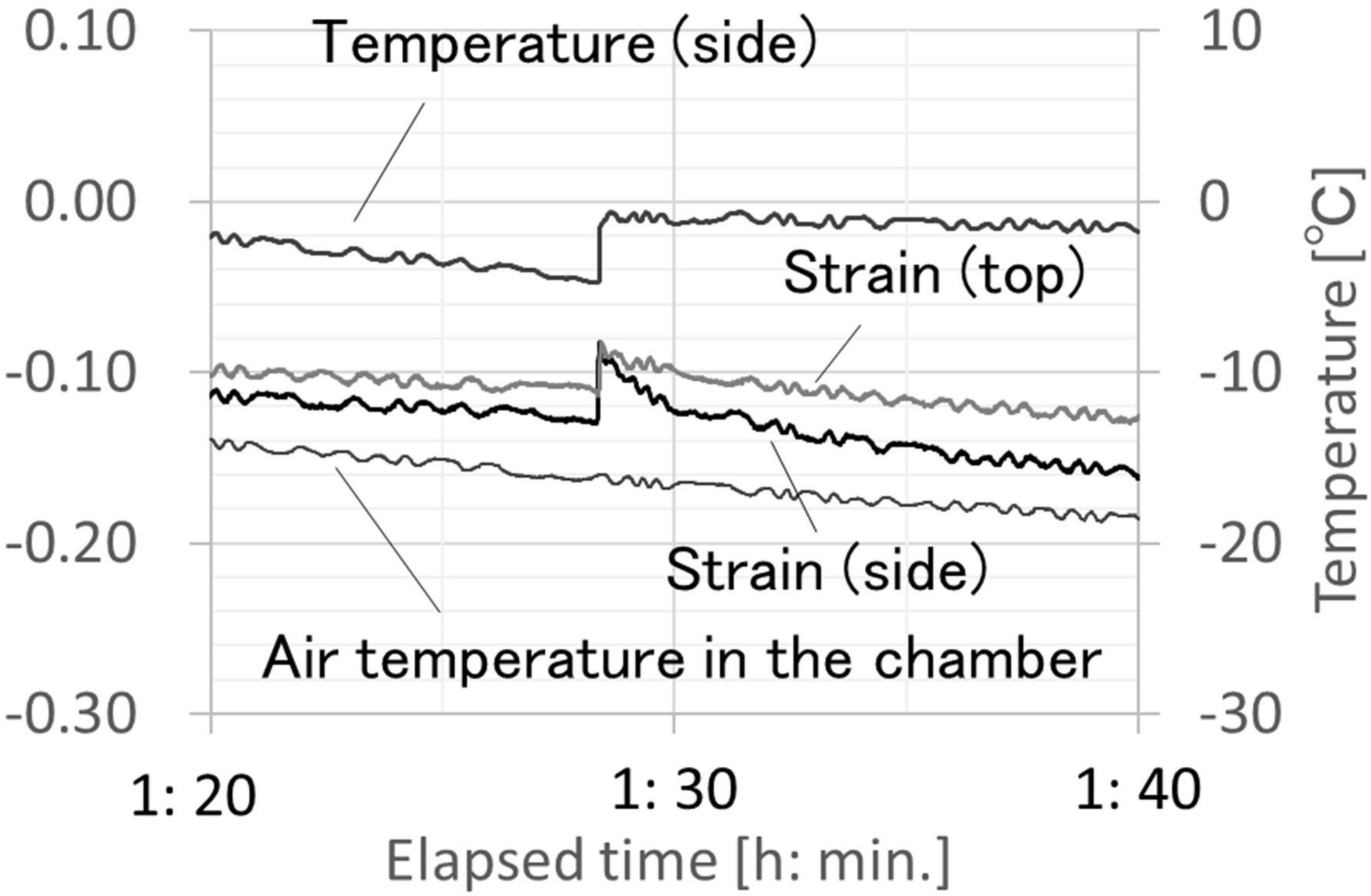
Temperature (side)
Strain (top)
Strain (side)
Air temperature in the chamber
Strain [10-3]
Temperature [°C]
Elapsed time [h: min.]
0.10
0.00
-0.10
-0.20
-0.30
10
0
-10
-20
-30
1: 20
1: 30
1: 40

(b)

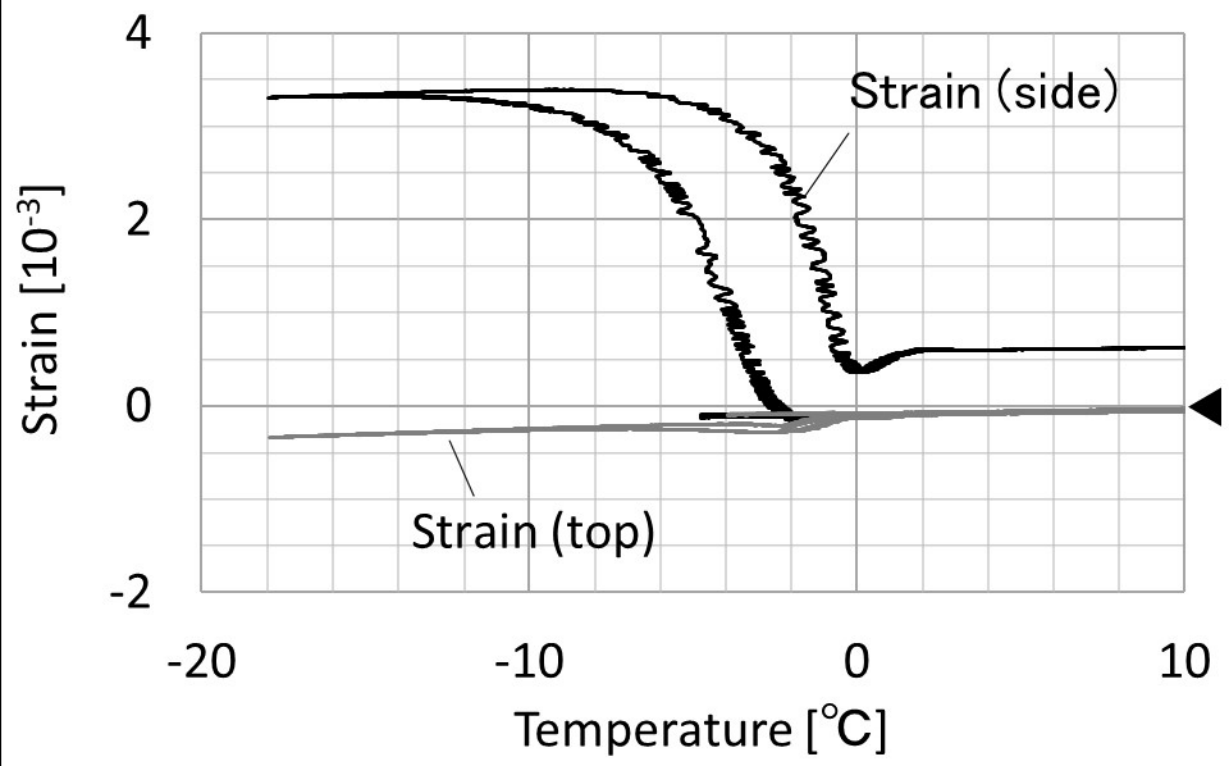
4
2
0
-2
Strain [10-3]
Strain (side)
Strain (top)
-20
-10
0
10
Temperature [°C]

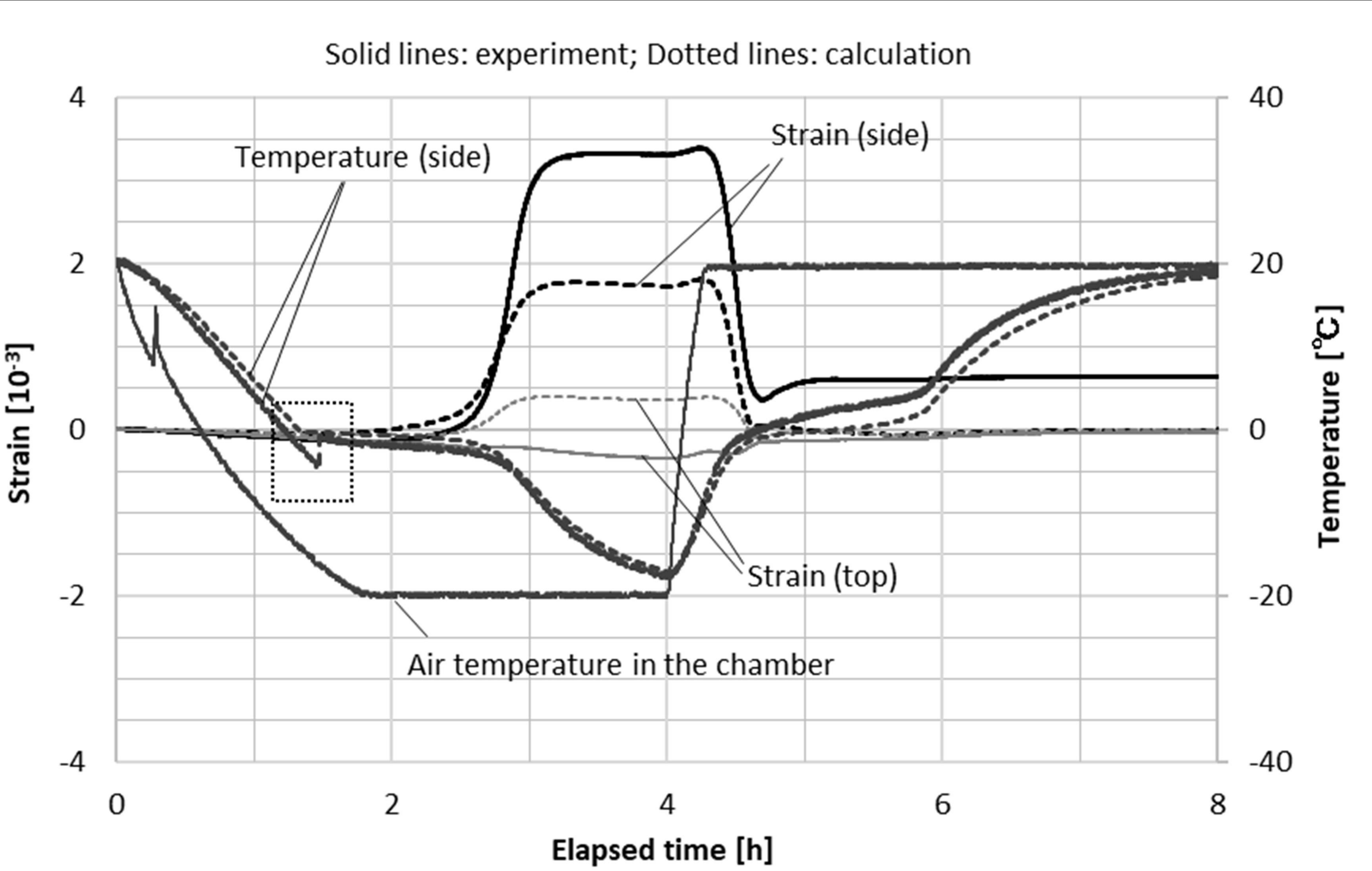
Solid lines: experiment; Dotted lines: calculation
Temperature (side)
Strain (side)
Strain (top)
Air temperature in the chamber
Strain [10-3]
Temperature [°C]
Elapsed time [h]
4
2
0
-2
-4
40
20
0
-20
-40
0
2
4
6
8

(a)

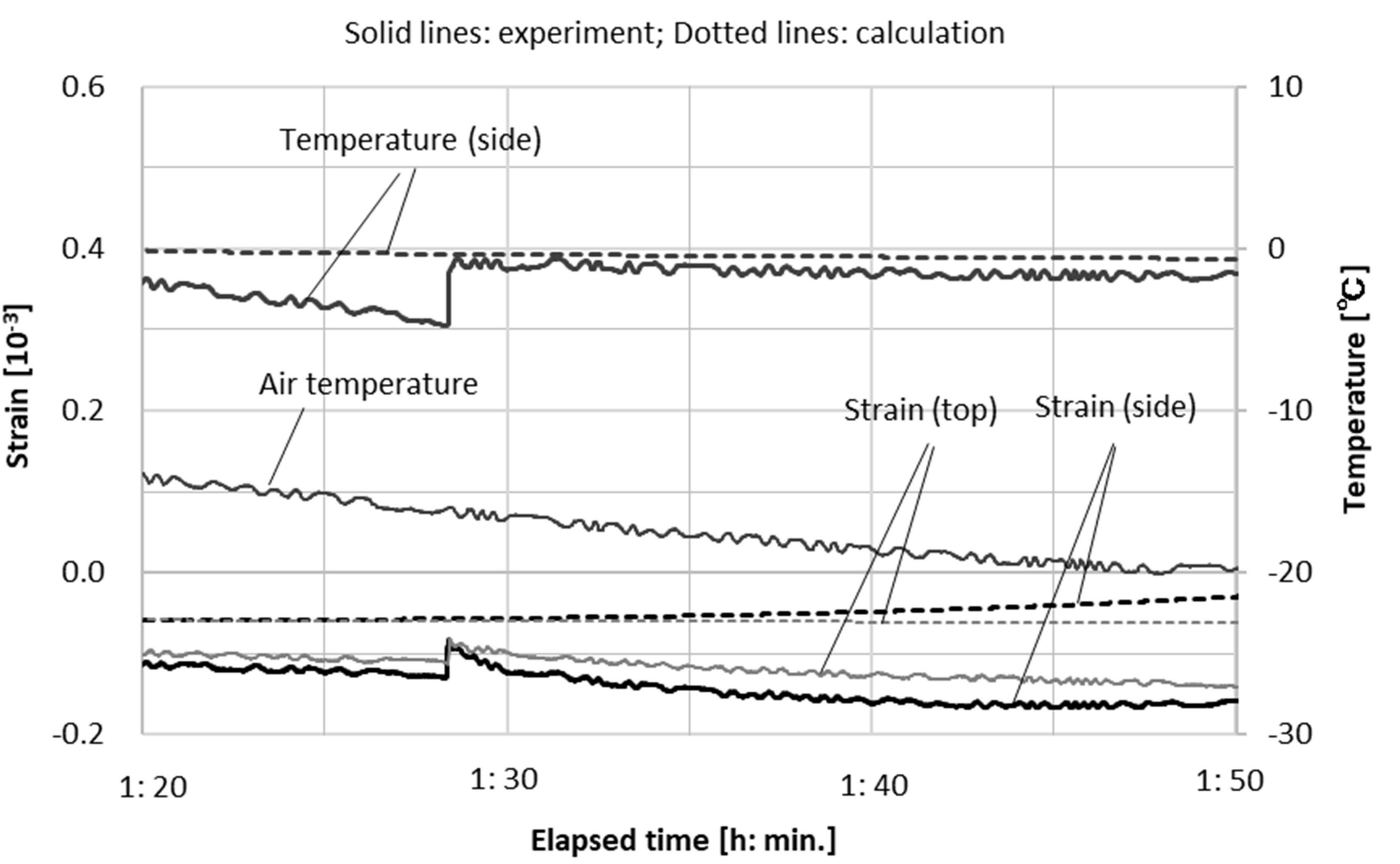
Solid lines: experiment; Dotted lines: calculation
Temperature (side)
Air temperature
Strain (top)
Strain (side)
Strain [10-3]
Temperature [°C]
Elapsed time [h: min.]
0.6
0.4
0.2
0.0
-0.2
10
0
-10
-20
-30
1: 20
1: 30
1: 40
1: 50

(b)

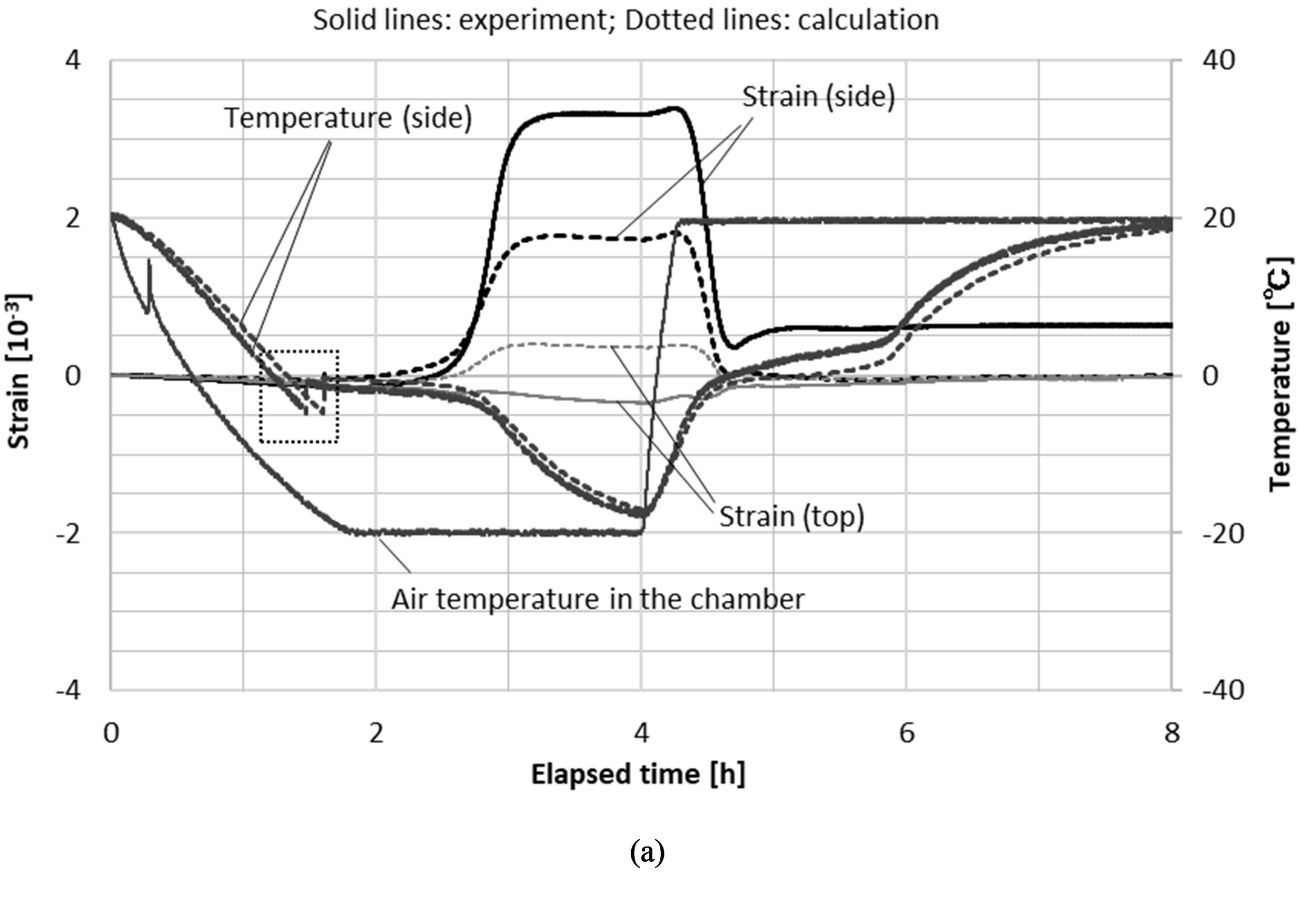
Solid lines: experiment; Dotted lines: calculation
Temperature (side)
Strain (side)
Strain (top)
Air temperature in the chamber
Strain [10-3]
Temperature [°C]
Elapsed time [h]
4
2
0
-2
-4
40
20
0
-20
-40
0
2
4
6
8

(a)

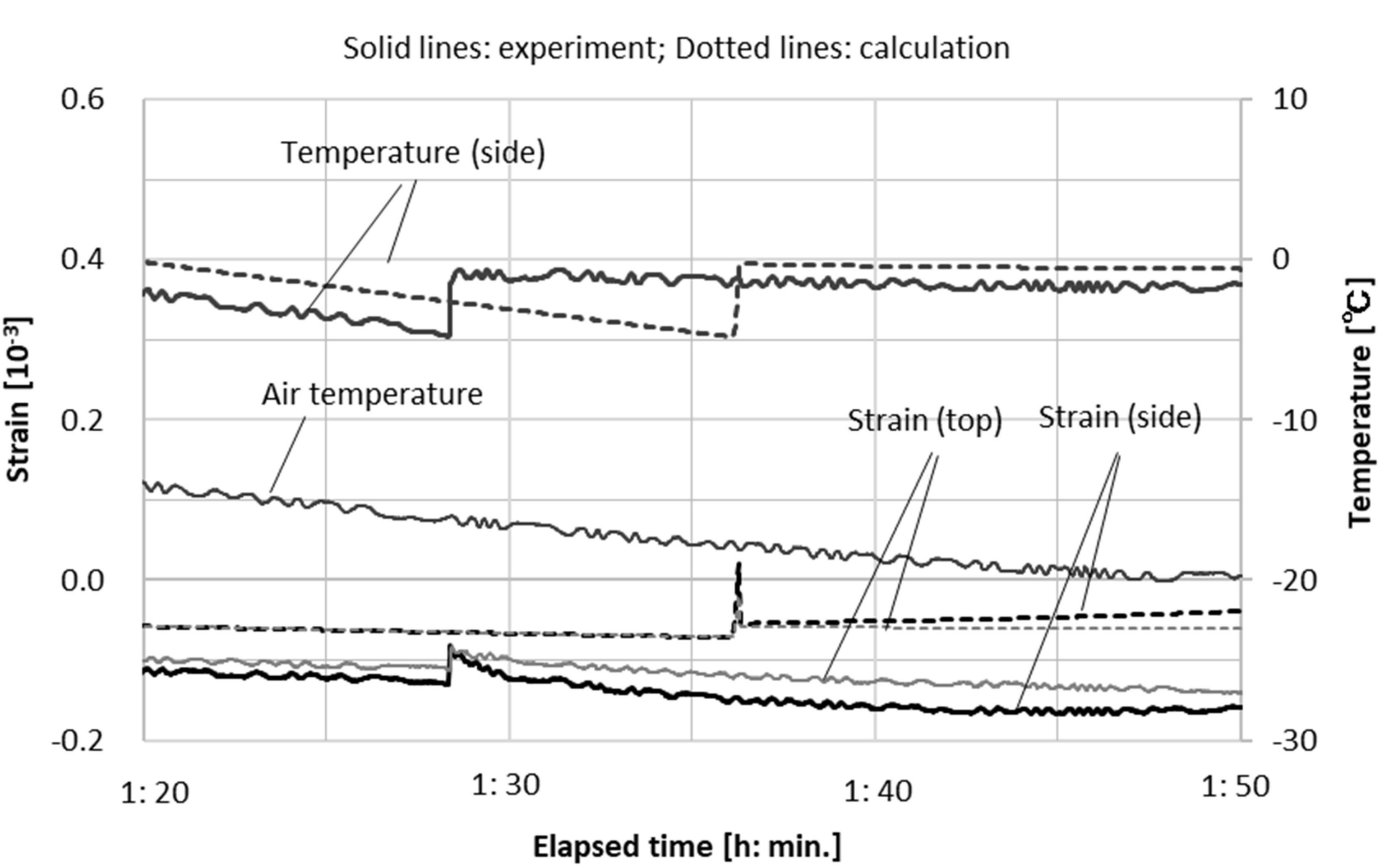
Solid lines: experiment; Dotted lines: calculation
Temperature (side)
Air temperature
Strain (top)
Strain (side)
Strain [10-3]
Temperature [°C]
Elapsed time [h: min.]
0.6
0.4
0.2
0.0
-0.2
10
0
-10
-20
-30
1: 20
1: 30
1: 40
1: 50

(b)

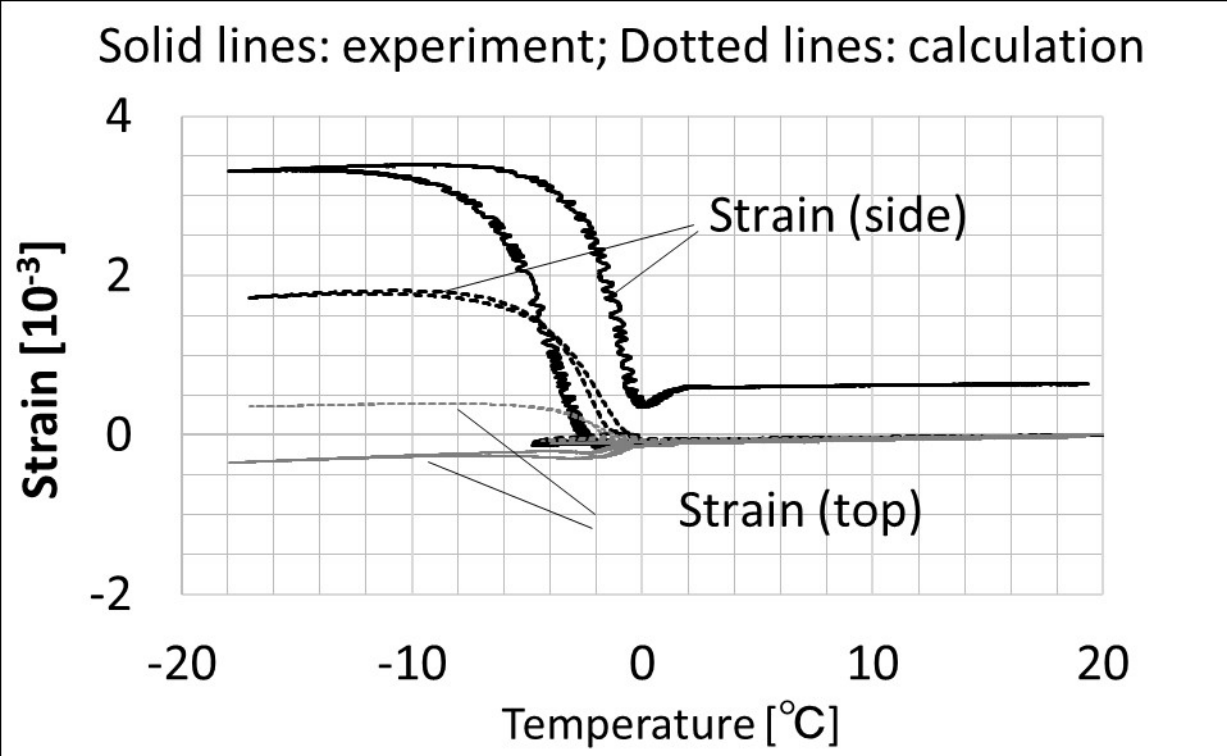
Solid lines: experiment; Dotted lines: calculation
Strain [10-3]
4
2
0
-2
Strain (side)
Strain (top)
-20
-10
0
10
20
Temperature [°C]

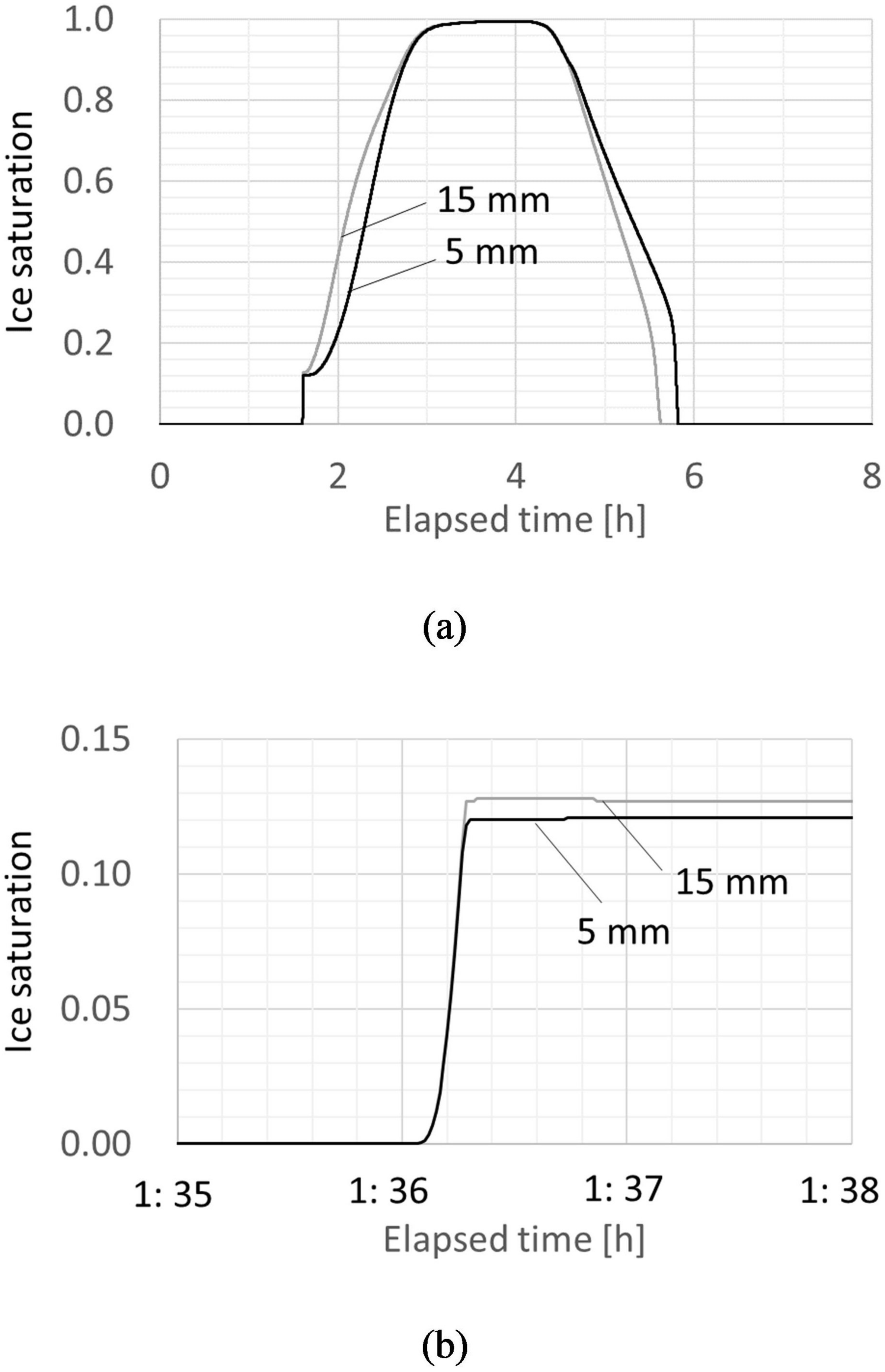
Ice saturation
1.0
0.8
0.6
0.4
0.2
0.0
15 mm
5 mm
0
2
4
6
8
Elapsed time [h]
(a)
Ice saturation
0.15
0.10
0.05
0.00
15 mm
5 mm
1: 35
1: 36
1: 37
1: 38
Elapsed time [h]
(b)

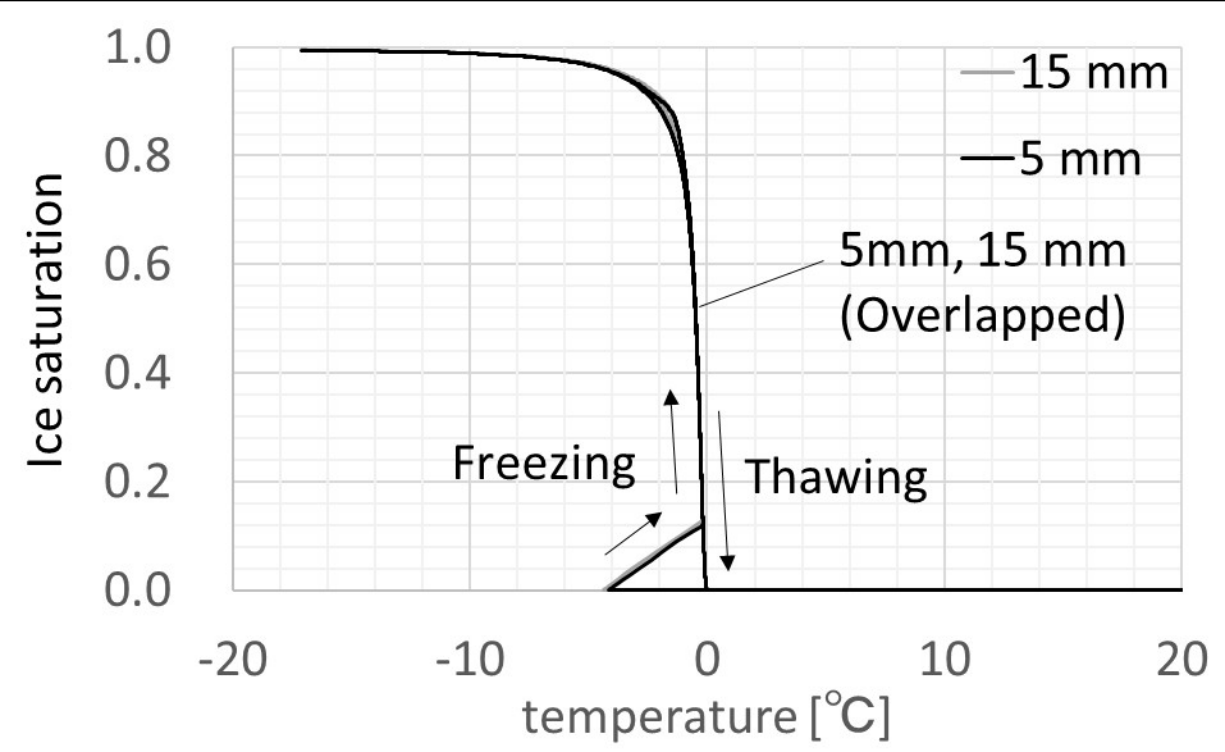
1.0
0.8
0.6
0.4
0.2
0.0
Ice saturation
15 mm
5 mm
5mm, 15 mm
(Overlapped)
Freezing
Thawing
-20
-10
0
10
20
temperature [°C]

Liquid water pressure [MPa]

6
5
4
3
2
1
0

$\lambda' \times 0.1$ (5 mm)

$\lambda' \times 0.1$ (15 mm)

$\lambda' \times 1$ (5 mm)

$\lambda' \times 1$ (15 mm)

1: 35
1: 36
1: 37
1: 38

Elapsed time [h: min.]

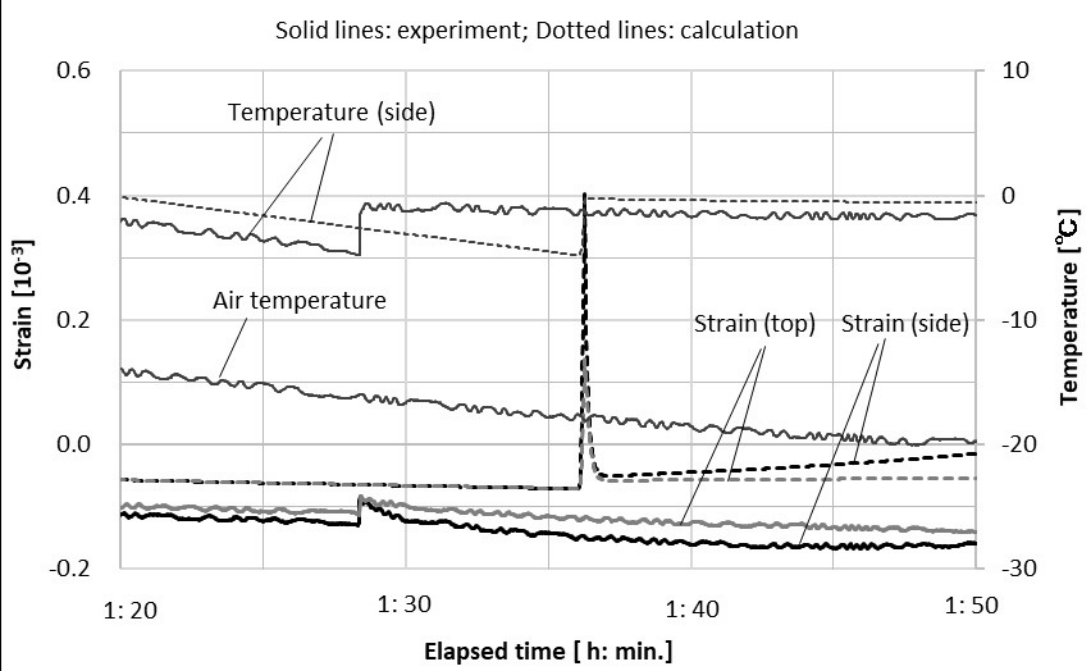
Solid lines: experiment; Dotted lines: calculation
Temperature (side)
Air temperature
Strain (top)
Strain (side)
Strain [10-3]
Temperature [℃]
0.6
0.4
0.2
0.0
-0.2
10
0
-10
-20
-30
1: 20
1: 30
1: 40
1: 50
Elapsed time [h: min.]

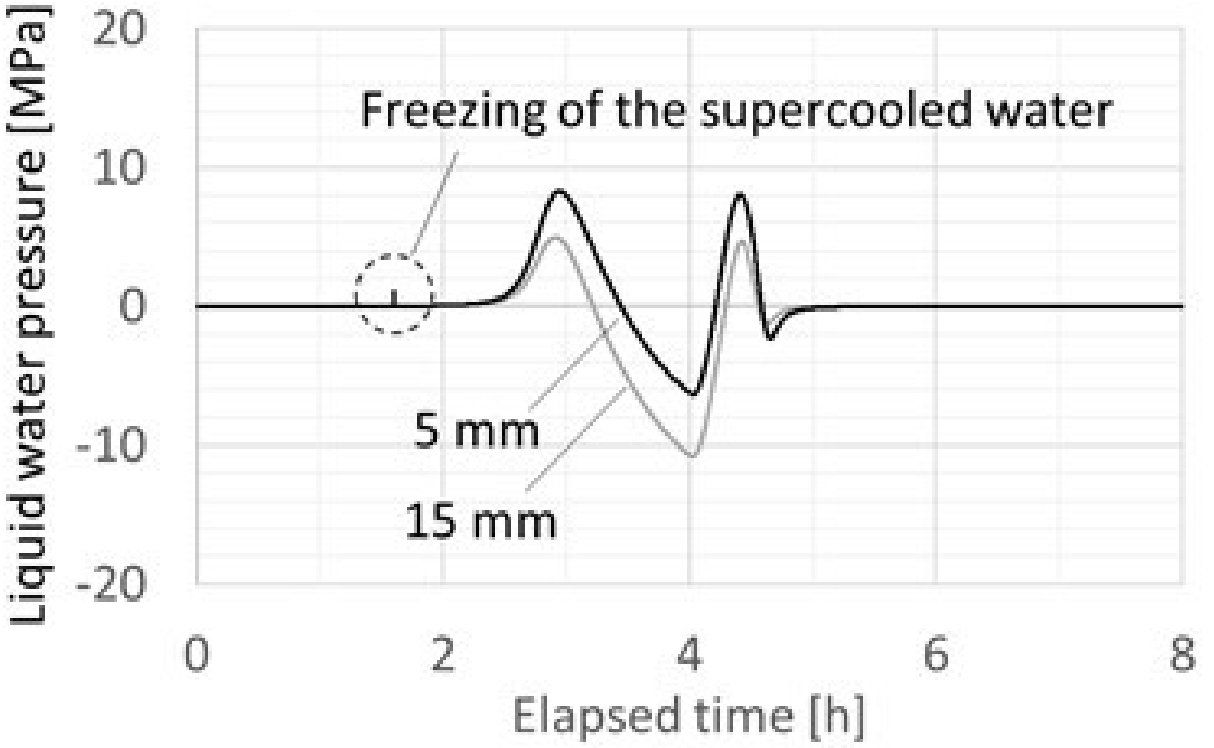
Liquid water pressure [MPa]
20
10
0
-10
-20
Freezing of the supercooled water
5 mm
15 mm
0
2
4
6
8
Elapsed time [h]

(a)

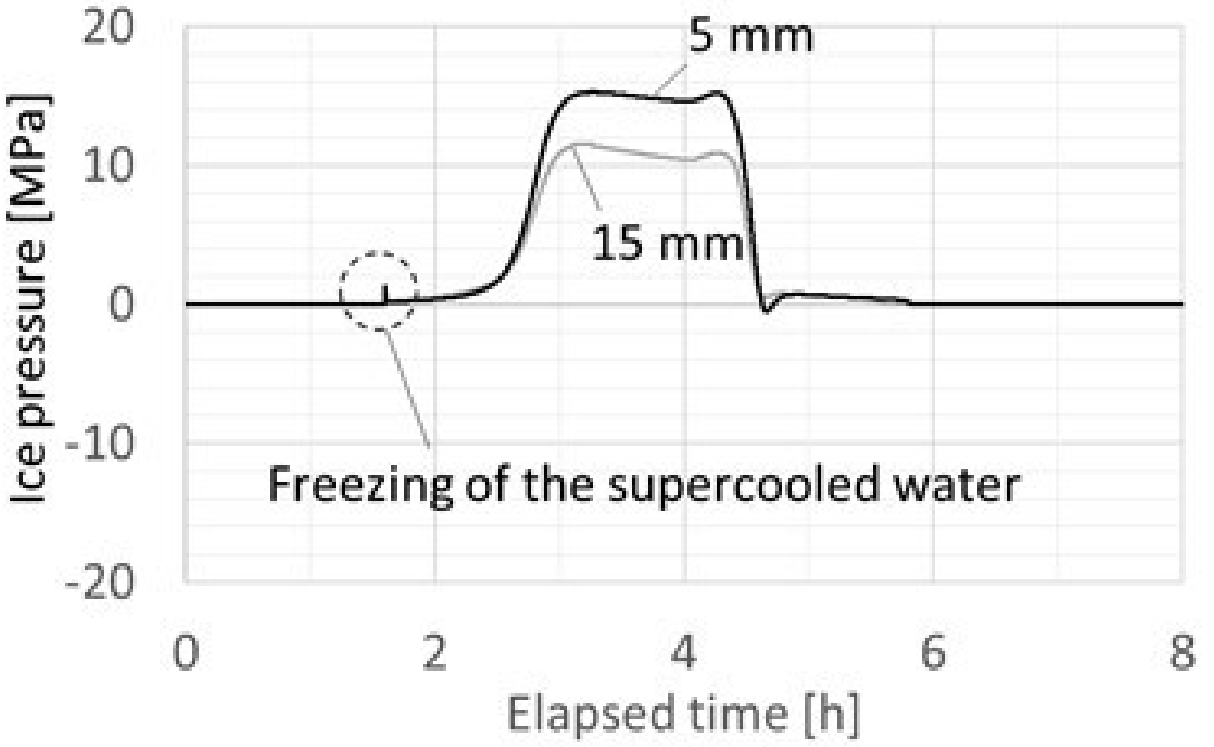
Ice pressure [MPa]
20
10
0
-10
-20
5 mm
15 mm
Freezing of the supercooled water
0
2
4
6
8
Elapsed time [h]

(b)